
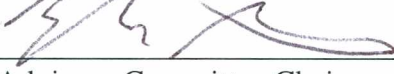


INVESTIGATION OF A TENSILE CYCLOIDAL ROTOR AND CAM CYCLIC
PITCHING MECHANISM

By


Kelsey H. Elfering

RECOMMENDED: 

Advisory Committee Chair


Chair, Department of Mechanical Engineering

APPROVED: 
Dean, College of Engineering and Mines


Dean of the Graduate School

May 16, 2012
Date

INVESTIGATION OF A TENSILE CYCLOIDAL ROTOR AND CAM CYCLIC
PITCHING MECHANISM

A
THESIS

Presented to the Faculty
of the University of Alaska Fairbanks

in Partial Fulfillment of the Requirements
for the Degree of

MASTER OF SCIENCE

By

Kelsey H. Elfering, B.S.

Fairbanks, Alaska

August 2012

Abstract

A cycloidal rotor is characterized by an airfoil span parallel to the axis of rotation. A tensile cycloidal rotor places the airfoils under tensile forces only, thereby attempting to utilize the inertial forces on the rotor to minimize airfoil deflection and overall weight. A prototype rotor was built that meets the micro air vehicle (MAV) size constraint of 15.24 centimeters (6 inches). A new cam path design was used as a pitching mechanism, which reduced overall design weight and mechanical power requirements, and allowed for curved flat plate airfoils and angled airfoil structural supports. The cycloidal rotor was designed to pitch on both sides of the airfoils in an effort to reduce the axial force that was previously observed in mechanisms that pitch straight airfoils using an offset four bar linkage on only one side. The radial and axial strains were measured to determine the forces on the rotor, and compared well with a finite element simulation. The power-to-thrust ratio increased with RPM, which is in contradiction with theoretical rotor predictions. This indicated there are likely inefficiencies due to friction, which is supported by the measured non-zero power requirement at zero RPM.

Table of Contents

Signature Page	i
Title Page	ii
Abstract	iii
Table of Contents	iv
List of Figures	vi
List of Tables	vii
1 Introduction	1
1.1 Problem Statement	1
1.1.1 Characteristics	1
1.1.2 Flow Conditions	1
2 Literature Review	2
2.1 Background	2
2.2 State of the Art	2
2.2.1 Wireless Pitch Control	2
2.2.2 Induced Camber	3
2.2.3 PIV: Particle Image Velocimetry	4
2.2.4 Control/Pitching Mechanisms	5
2.2.5 Vibration/Friction	6
2.3 Airfoil Cross-Section	6
3 Cycloidal Rotor Design	8
3.1 Theory	8
3.2 Rotor Size	8
3.3 Angle of Attack	8
3.4 Number of Airfoils	9
3.5 Reynolds Number and Taper	9
3.6 Chord Length	9
3.7 Flat Plate Airfoil Profile	10
3.8 Cyclic Pitching Mechanism	11
3.9 Design of the Entire Rotor	15
4 Structural Analysis	17

4.1	SolidWorks Simulation	17
4.1.1	Airfoil Stress/Displacement	17
4.1.2	Structural Support Stress/Displacement	18
5	Rotor Prototyping and Manufacture	21
5.1	Spider Support Compression Molds	21
5.1.1	Material	22
5.1.2	Bending Jig	22
5.1.3	Spider Arm Dimension	23
5.1.4	Displacement Pins.....	23
5.2	Airfoil Compression Molds.....	24
5.3	Programmable Furnace	24
5.4	Cyclic Pitching Mechanism	24
5.5	Hardware	25
5.6	Spider Supports, Airfoils, and Final Assembly.....	26
5.7	Motor, Controller, and Speed Control.....	28
6	Experimental Testing	29
6.1	Apparatus	29
6.2	Pitch Mechanism Test	30
6.3	Total Power and Strain Testing.....	31
7	Results and Discussion	35
7.1	Thrust and Axial Force.....	35
7.2	Cycloidal Rotor Comparison.....	37
7.3	Conclusions	39
7.4	Further Consideration.....	40
8	References.....	41
	Appendices.....	42

List of Figures

Figure 1: Acuity Technology Pressure Visualization (Clark R. , 2006).....	3
Figure 2: From Seoul University analyzing induced camber effects and calculated/predicted thrust forces with respect to angle of attack.	3
Figure 3: PIV by Moble Benedict at the University of Maryland, Department of Aerospace.....	4
Figure 4: Shear Potential for Angle of Attack Mechanism from Seoul University.....	5
Figure 5: Example of mechanical offset to achieve variable angle of attack with a pitch link. (Chopra, 2011).....	6
Figure 6: Darrieus rotor with variable chord length and thickness to increase power generation (Clark R. , 2008).	7
Figure 7: Thrust versus RPM and Aerodynamic Power versus Thrust.	9
Figure 8: A SolidWorks 2011 model showing the chosen geometry of the structure supporting the airfoils with parallel oscillating pulleys for one to one pitching.	10
Figure 9: A cross-section view showing how the cyclic pitching mechanisms will be installed.....	11
Figure 10: The cyclic pitching mechanism which represents an offset disk of an offset four bar method.....	12
Figure 11: Two dimensional representation of the cyclic pitching mechanism. The angle of the pegs with respect to the center of the base pulleys is $\pm 40^\circ$ for the top and bottom and 0° on the side.	13
Figure 12: The pitching mechanism with the base pulleys and oscillating pegs are shown in cyclic pitching.	14
Figure 13: SolildWorks 2011 full design model.....	15
Figure 14: Plots of the displacement (top) and Von Mises stress (bottom) under a uniform load (purple arrows) that represents the thrust force during rotation. The displacement shown exaggerated for better visualization. Maximum displacement is 2.8 mm near the center (red).	17
Figure 15: Displacement of the spider structural support under equal loading on all four arms. Maximum displacement occurs on the edge of the arm and 0.1278 mm..	18
Figure 16: Structural Support with loading that is more realistic with two of the arms attached to the airfoils with ± 40 degrees with more load due to drag and, thrust than the non-pitched airfoil arms.....	19
Figure 17: Stress in the structural supports under larger than necessary conditions. ..	19
Figure 18: Fatigue analysis of increased loads on the main components of the rotor.	20
Figure 19: Compression molds shown with pegs and center location hole as well as an angled hole for pulley support drilling.....	21
Figure 20: Bending Jig used to create specified angles in the spider support compression molds.....	22

Figure 21: Test specimen of two 3.175 mm heat treated aluminum with 1.5875 mm in the middle where the carbon fiber arms will be determining the differential length needed in the arms.	23
Figure 22: Sprue tree with lost wax casting bronze pitching mechanism.....	24
Figure 23: Additional hardware used for the pulley mechanism, showing a progression of assembly from right to left.	25
Figure 24: Carbon fiber spider supports with bearings inserted.	25
Figure 25: Two views of the carbon fiber airfoil geometry.	26
Figure 26: The final completed assembly with the rotor mounted to the test stand and meshed with the motor's pinion gear.	27
Figure 27: Demonstrating the pitching of the airfoils to the designed $\pm 40^\circ$	27
Figure 28: Spinning cycloidal rotor to perform force and power testing.	29
Figure 29: LabVIEW block diagram for acquiring and storing the strain data as a function of time while testing the rotor.	30
Figure 30: Plot showing experimental power consumed by both pitching mechanisms as a function of RPM.	31
Figure 31: The pitching mechanism power versus the cube of the RPM with an R^2 correlation of 0.9874.	32
Figure 32: Plot showing the power as a function of RPM for the entire rotor assembly compared to that of just the pitching mechanisms.	33
Figure 33: Plot of the relationship of the total power (R^2 correlation of 0.9821) and the pitch mechanism power (R^2 correlation of 0.9874) versus the cube of the RPM. .	33
Figure 34: The measured strain values for the axial and radial directions for variable RPM.	34
Figure 35: SolidWorks strain analysis of vertical distributed load on the rod.....	35
Figure 36: Plot showing the radial (thrust) and axial forces on the cycloidal rotor as a function of RPM.	36
Figure 37: Plot of the two perpendicular forces, thrust (R^2 correlation of 0.9967) and axial force (R^2 correlation of 0.9857) on the rotor as a function of the RPM squared	36
Figure 38: Relationship for total power and thrust as RPM varies.	39

List of Tables

Table 1: Showing the performance and geometry of some previous cycloidal rotors designs. Table adapted from the University of Maryland, Department of Aerospace (Chopra, 2011).	37
--	----

List of Appendices

Appendix A:.....	42
Appendix B:.....	45

1 Introduction

1.1 Problem Statement

Micro Air Vehicles (MAVs) are highly sought after for their low energy consumption surveillance, patrolling, and reconnaissance capabilities for both civilian and military purposes. MAVs are defined by the Defense Advanced Research Projects Agency (DARPA) as having a characteristic length of no more than 15.24 cm (6 inches). This interest has caused a surge of analysis and research in recent years. Helicopters conventionally appear to be the best solution. A helicopter is a successful aerodynamic vehicle that has been optimized for full scale conditions. However, MAV helicopters are half as efficient compared to full scale helicopters in terms of the ratio of actual to ideal power (McMichael, 1997).

1.1.1 Characteristics

Ideal characteristics include hovering, fast takeoff and landing, good maneuverability, endurance, and stability in adverse weather conditions such as wind. Efficiency is a key attribute for minimal power consumption with maximum thrust. Conventional rotors are less efficient in terms of power-to-disc loading compared to a cycloidal rotor (Benedict, 2011). Efficiency clearly affects the flight distance per battery charge and the power consumption. These aspects of flight are hard to increase due to rotor and component weights and power to battery weight ratios at the MAV scale.

1.1.2 Flow Conditions

A cycloidal rotor with a diameter of 15.24 centimeters, operating at 2000 RPM would experience a Reynolds number of 322,000. The flow conditions have been of much interest in recent years. Complex phenomena like dynamic stall and induced camber have been believed to be contributing factors to explain why cycloidal rotors have never reached stall, as well as being pitched to large angles of attack. The interactions between cycloidal airfoils have also been investigated because large chord lengths may lead to inefficiencies and unpredictable performance as the airfoils pass closer together.

2 Literature Review

2.1 Background

The first pictures of the cycloidal rotor concept were over a hundred years ago in Russia from 1906. Several patents from the early part of the 20th century were processed. Frederick Kurt Kirsten first investigated cycloidal propulsion in the early 1920's while working at the University of Washington and proposed to replace an aircraft's airfoils with those of a cycloidal rotor, but the aircraft crashed first (Kirsten, n.d.). In 1926, H. Sachse stated that Boeing helped Kirsten in the invention and experimentation of the cycloidal rotor in NACA No. 351 and notes the key advantage is instant thrust vectoring.

John B. Wheatley began work on cycloidal propulsion in 1933 and developed a supporting model from tests at the Langley 20-foot wind tunnel using an 8-foot diameter model. Wheatley also provided a simplified analysis of this general system by varying design parameters to produce a performance model. He concluded that a cyclogiro was competent in all forms of flight and could even glide in the case of power failure (Wheatley, 1933). Primary interest until the 1990's was focused on tug boats until interest in MAVs became prevalent, and lightweight materials with high strength that can withstand high speed became more available.

Since this early development, there have been numerous research theses and projects that range from purely computational analyses to rotor development and testing. One successful endeavor by the Aerospace Department of the University of Maryland created the first remote flight controlled cycloidal MAV in 2011. Starting in 2008, Chopra and Benedict published many research papers analyzing the nature of cycloidal rotors and iteratively refined their experimental rotor until a working model was achieved with near instant thrust vectoring (Chopra, 2011).

2.2 State of the Art

Current cycloidal rotor technology utilizes small radii of rotation due to the massive increase in perceived weight due to centripetal force, or in low RPM scenarios that require a lot of thrust to move heavy loads. The latter is employed by tugboats that are required to pull many times their own weight when moving larger vessels.

2.2.1 Wireless Pitch Control

Cycloidal airfoil research has found thrust efficiencies ranging from 14 grams of thrust per watt at full scale; and these experiments and research indicated the thrust to power ratio may double that of current helicopter technology (Wheatley, 1933). Most cycloidal research has consisted of airfoils with constant direction of rotation and variable angle of attack as the airfoils make a full rotation from $\pm 40^\circ$ for optimal thrust. Figure 1 shows a numerical simulation of the pressure regime around a

pitched airfoil, created by Acuity Technology Proprietary using Chimera Grid Tools, Overflow 2.0, Tecplot, and Matlab. Acuity Technology did successfully transmit wireless signals to servos to control the angle of attack on cycloidal airfoils for accurate sinusoidal pitching analysis. Higher pressure is shown in red, where lower pressure is in blue.

The bottom airfoil would have a negative angle of attack when the rotation is counterclockwise, while the top airfoil has a positive angle of attack with respect to the leading edge of the airfoils. The top and bottom airfoils generate net thrust in the upward direction; generating thrust in one direction by two airfoils simultaneously. This type of motion is characterized as a periodic stroke and is beneficial towards positive thrust. As both airfoils rotate counterclockwise 180 degrees to switch locations and angle of attack the airfoils will pass through a neutral angle of attack. The bottom airfoil's gradient from high to low pressure is not as significant as the top airfoil suggesting that it produces less thrust.

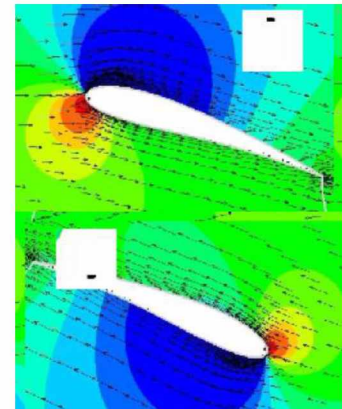


Figure 1: Acuity Technology Pressure Visualization (Clark R. , 2006)

2.2.2 Induced Camber

A symmetrical airfoil is often used for cycloidal rotors, but the airfoils act as if they are cambered because the path that is traveled is curved in a circle with respect to the span. This effect is considerable because the radius of curvature is relatively small compared to the chord length of the airfoils. This phenomenon is called virtual or induced camber because the airfoils are not actually cambered, but do behave as if they are. Figure 2 (left) shows analytical, experimental and CFD data for force versus angle of attack for 300, 400, and 500 RPM. The force increases with higher RPM at

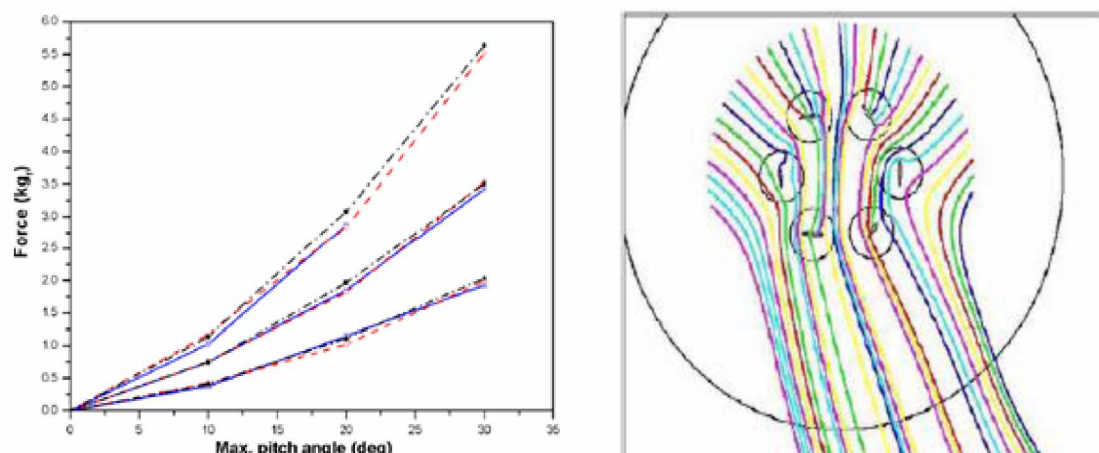


Figure 2: From Seoul University analyzing induced camber effects and calculated/predicted thrust forces with respect to angle of attack.

all angles of attack and low RPM values were used to maintain laminar flow conditions. Streamlines are shown on the right in Figure 2. Of considerable note from this flow visualization is the direction of outward flow from the bottom of the rotor. This six bladed rotor's flow is offset 20° from the vertical (where maximum angle of attack is achieved) not directly downward as might be expected (Kim, 2008). For a four bladed rotor this angle of flow diversion is 15° .

2.2.3 PIV: Particle Image Velocimetry

Particle Image Velocimetry (PIV) uses injected particles into a fluid velocity field as an optical method to obtain instantaneous velocity measurements. Figure 3 shows PIV measurements made by Moble Benedict at the University of Maryland, Department of Aerospace. On the left; arrows indicate velocity direction and red to blue colors are used to represent greater to lesser magnitudes respectively. This also agrees with the visualization of flow in Figure 2 that has the outward flow directed at an angle from the vertical. PIV tip vortices shown on the right, use red and blue to signify counterclockwise and clockwise rotation of vortices, respectively. This flow visualization method can be used to calculate the circulation, which can then be used to find the overall thrust of a rotor.

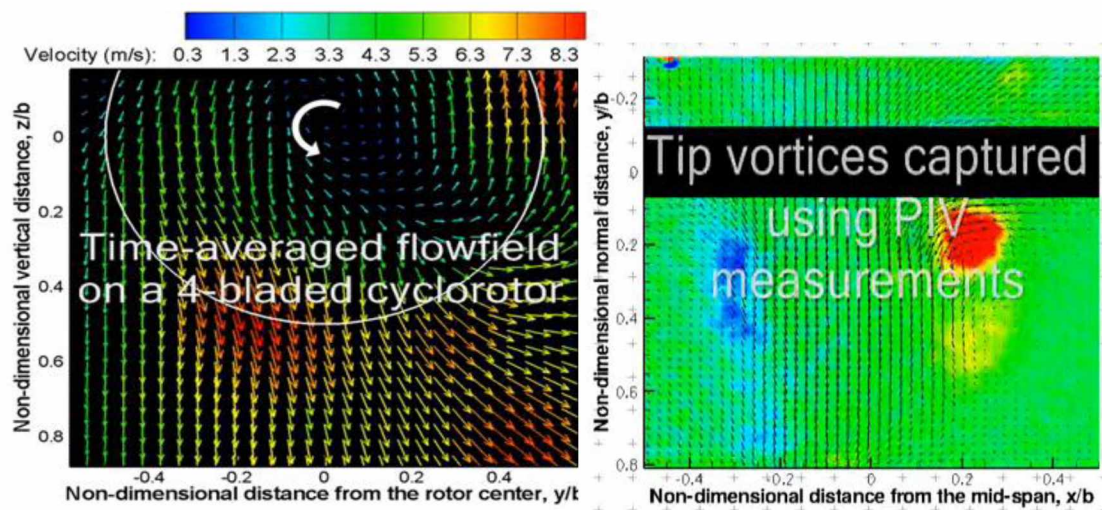


Figure 3: PIV by Moble Benedict at the University of Maryland, Department of Aerospace.

2.2.4 Control/Pitching Mechanisms

Shear stresses in current cycloidal rotor designs cause substantial size constraints on horizontal axis rotors. Conventional horizontal rotor airfoils are a solid structure, and at high velocities can lead to great damage to the supporting structure and angle of attack mechanisms. Figure 4 shows that MAV models have demonstrated that damaging effects can occur from controlling the angle of attack. Critical stress is shown on the right in red for the control link in the airfoil on the left (Kim, 2008).

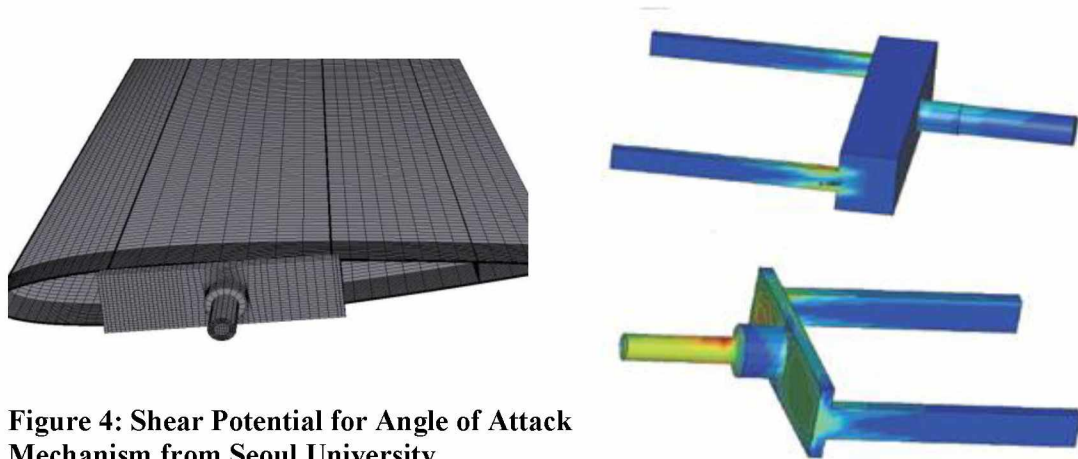


Figure 4: Shear Potential for Angle of Attack Mechanism from Seoul University

One approach is to have each airfoil controlled by servo technology for exact sinusoidal angle of attack, but this is used for static experimentation for ideal performance as discussed in Section 2.2.1. This is because the numerous electronics have considerable weight when combined. There is also a more simple mechanical approach. Cycloidal rotors rotate around a central axis denoted as the x-axis, and the pivot point of oscillation for the airfoils occur at the quarter-chord. The axis of rotation for the pitching mechanism is parallel, and an offset distance to the central axis. The four bar pitching mechanism connects to the airfoils a set distance from the quarter chord of the airfoils. Figure 5 demonstrates a four bar pitching mechanism using a titanium rod set in foam with a carbon fiber layer to reinforce the airfoils to maintain a constant angle of attack along the span (Chopra, 2011).

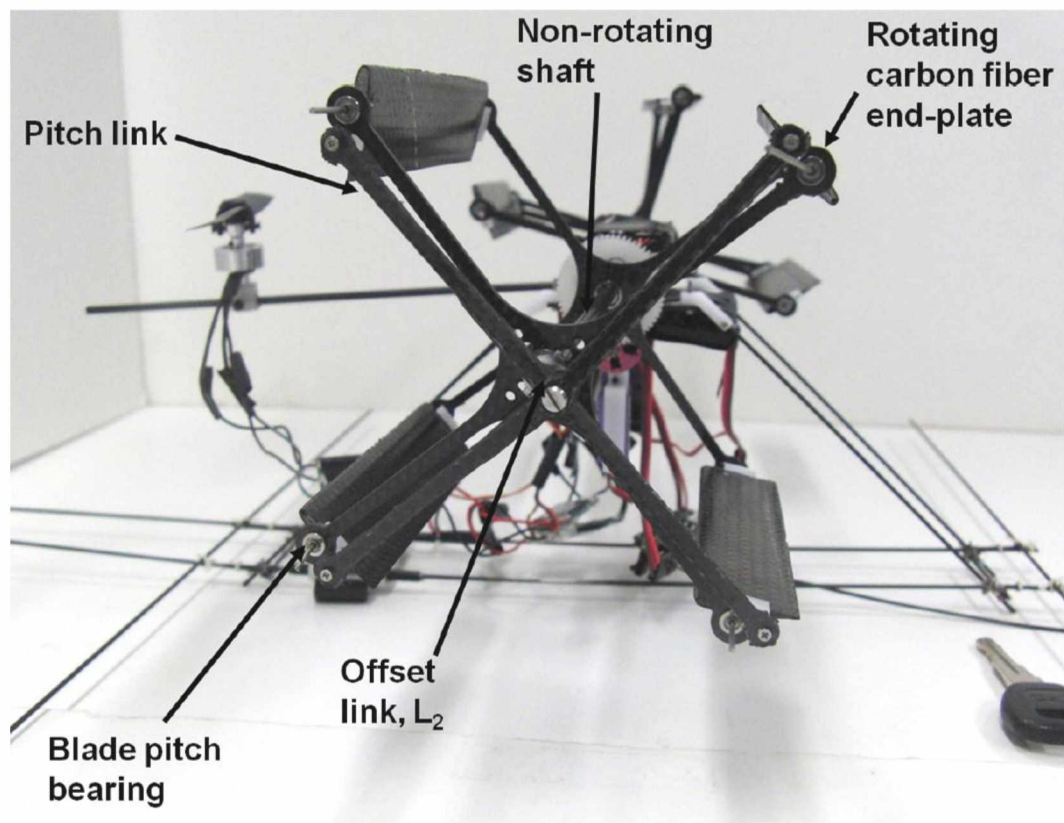


Figure 5: Example of mechanical offset to achieve variable angle of attack with a pitch link. (Chopra, 2011)

2.2.5 Vibration/Friction

High centripetal force causes any amount of unbalanced weight to cause a large amount of vibration of the same order of magnitude as the thrust from a cycloidal rotor. Even with a small rotor balanced tolerance within 0.02 grams mass difference between components achieved vibration two orders of magnitude greater than the thrust that was measured (Parsons, 2005).

2.3 Airfoil Cross-Section

A cycloidal rotor resembles a vertical axis wind turbine (VAWT) rotated ninety degrees on its side, which is why it is categorized as a horizontal axis rotor. Figure 6 shows a design of a Darrieus Rotor with variable chord length. It was able to operate at higher RPM than a straight airfoil VAWT with similar radius and incoming air speed. The experimental data showed similar Reynolds number along the span of airfoils with variable chord length. This achieved similar flow conditions along the span of the airfoils.

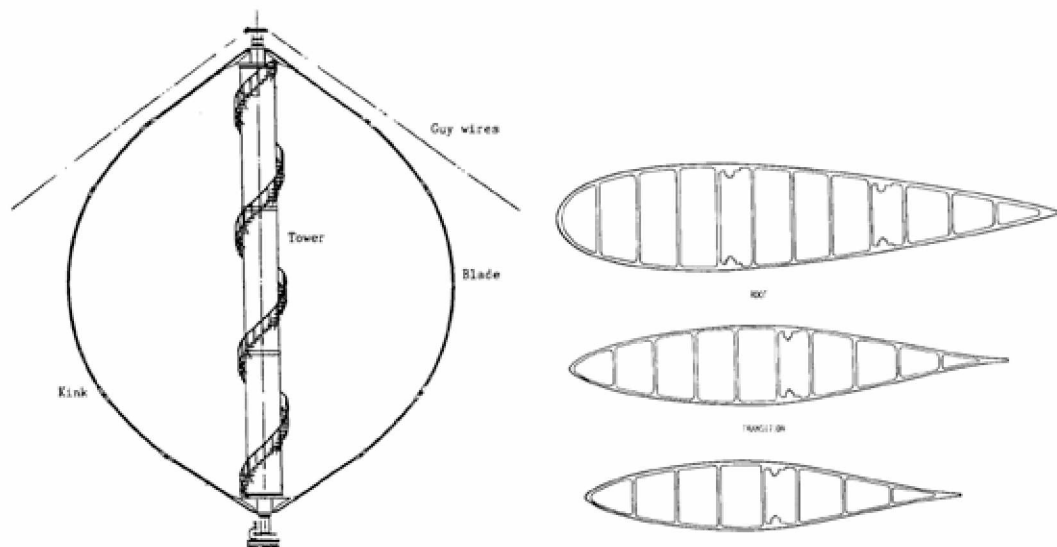


Figure 6: Darrieus rotor with variable chord length and thickness to increase power generation (Clark R. , Design and Initial Performance of a 500-kW Vertical Axis Wind Turbine, 2008).

This allowed for the rotor to operate seven times faster than a non-varying chord length Darrieus rotor and a 40% increase in power generated (Clark, 2008). These two features added to the design involved a cylindrical airfoil with respect to the span and chord length taper. The center of the airfoil is located the furthest from the horizontal axis and has the smallest chord length.

3 Cycloidal Rotor Design

3.1 Theory

A working cycloidal rotor at the micro air vehicle size was constructed and tested by (Benedict et al., 2008). The rotor was successful in being able to lift itself, but did not perform with maximum efficiency. An aerodynamic axial force that was of the same order of magnitude as the thrust was observed. This force was measured and confirmed by digital particle image velocimetry, DPIV, where skewed air flow was observed (Benedict et al., 2008). This rotor's airfoils were pitched on only one side of the rotor, resulting in a small amount of torsion in the airfoils. This rotor also implemented flat plate airfoils resulting in greater torsion and increased inefficiency. This torsion is believed to be the cause of the skewed air flow that was observed in the DPIV. To minimize this torsion the airfoils were made with foam core and a pitching spar of titanium with a layer of carbon fiber for reinforcement (Benedict et al., 2011). However, if the airfoils are pitched on both sides of the rotor the torsion of the airfoils may be reduced, and minimize the axial force and allowing for the use of a flat plate airfoil.

3.2 Rotor Size

There are size constraints in order for the rotor to be classified as a MAV. The diameter between airfoils revolved around the horizontal axis cannot be more than 15.24 cm. An average diameter of 12.7 cm was chosen at the angle of rotation where the airfoils have no pitch. This permitted the distance between the trailing and leading edges of the negative and positive pitched airfoils to be less than the 15.24 cm constraint. Therefore, there is 2.75 cm deviation for the airfoils to pitch. The length of each airfoil also has to be less than 15.24 cm to meet the MAV definition. Making the curved length of the airfoil to be 12.7 cm meets this constraint. This completed the geometry of the span of the airfoils as a cylindrical curve is applied; and calculated the radius of curvature of the airfoils to be 8.4836 cm.

3.3 Angle of Attack

The amount of pitch (or angle of attack) will be 40° from the zero pitch plane in the positive and negative directions, as shown in Figure 1. This magnitude of the pitch has been investigated by several institutions. Figure 7 on the left, shows that additional pitch above 40° no longer gives additional thrust, but does require additional power, as shown in Figure 7 on the right (Benedict, et al. 2008).

Therefore there is a ceiling of the angle of attack that is practical. Using a lower angle of attack and higher RPM is less efficient and was not investigated here. The loss in efficiency is because a sub- 40° angle of attack produces less thrust at all RPM. The aerodynamic power and thrust (vertical force) of the 40° and 45° are plotted nearly on top of each other in Figure 7. Therefore 40° was chosen as the angle of attack because it requires less aerodynamic and mechanical power than a pitch of 45° .

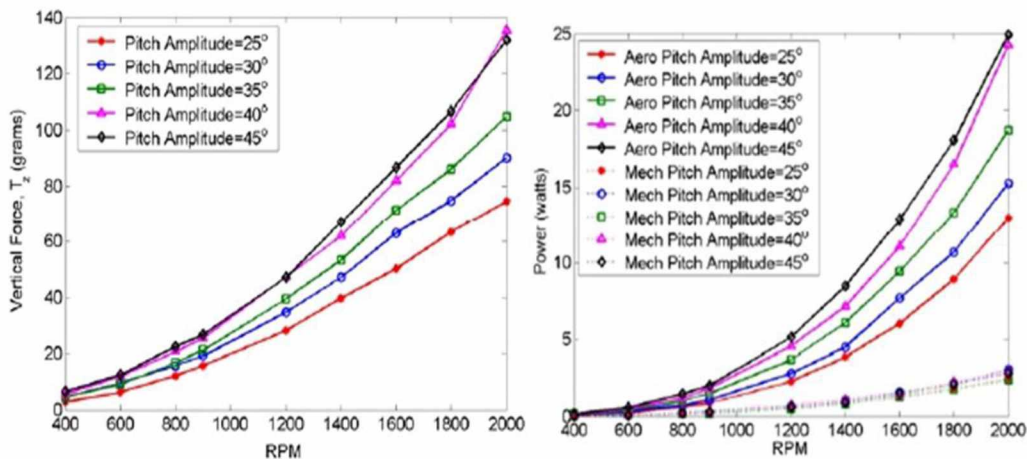


Figure 7: Thrust versus RPM and Aerodynamic Power versus Thrust.

3.4 Number of Airfoils

The number of individual airfoils on a single rotor has also been investigated previously. Intuitively a smaller number of airfoils have less inertial force and weight; however experiments have shown that two airfoils yield a pulsing of thrust (Parsons, 2005). This is an undesirable effect because a constant thrust for a given RPM of the rotor is required for dependable flight. The pulsing is minimized to an acceptable magnitude when four airfoils are utilized. When more than four airfoils are used, the effect of added thrust does not justify the added inertial force and structural weight. Moving from four to six airfoils is not worth the additional power required and the flow effects from one airfoil to another can be problematic; when the preceding airfoil can cause considerable downwash making the following airfoil less effective at the MAV scale (Parsons, 2005).

3.5 Reynolds Number and Taper

Fixing the cylindrical geometry of the airfoil with respect to the span allowed the taper to then be calculated. The taper is defined by measuring the deviation of chord length from connection of the spider supports to the airfoil to the middle of the airfoil. The chord length increases symmetrically from the middle of the airfoil to the edges connected to the spider supports. The local Reynolds number is defined as $Re = \frac{UL}{\nu}$, where L is the chord length at a location along the airfoil, and U is the linear velocity. The middle of the airfoil has a larger U than the spider connections of the airfoils because of an increase in distance from the axis of rotation. The change in U is proportional to a change in RPM. In order to maintain a constant Re , the characteristic length has to change in proportion to the changing U , and was accomplished by tapering the airfoils. The taper is not constant because the airfoils are bent in a circular arc from the two supports. For this variation in radius from the axis of rotation of 1.693 cm; the chord length taper is 0.508 cm from one end to the middle of the airfoil.

3.6 Chord Length

The chord length was determined by considering the trade-off between one that produces adequate thrust, but is small enough to have minimal drag and downwash

effects on the following airfoil. In 2003, Isosilevskii and Levy of the Technion-Israel Institute of Technology experimented with a similarly sized rotor of 10.922 cm diameter and a chord length of 2.286 cm. A computational fluid dynamic, CFD, study showed the complex flow field experienced by the cycloidal rotor due to the interaction between the airfoils, which was not previously expected. The model was tested with two, four, and six airfoils, and numerical predictions agreed with experimentally measured time-averaged forces. It was found by experimental analysis of different chord lengths that 2.286 cm was successful for a cycloidal rotor of the MAV scale. This chord length has also been successful for other cycloidal rotors. The chord length provides enough thrust and separation between airfoils for limited downwash effects.

3.7 Flat Plate Airfoil Profile

It has been shown by Benedict et al. (2008) that at the MAV scale a flat plate produces just as much thrust as an airfoil shape without any increase in aerodynamic power requirement. In their work the weight of the flat plate was substantial because a large thickness was required so there would be no torsion as the rotor was cyclically pitched on just one end. In the present work, a flat plate has been adopted as shown in Figure 8 because the rotor will be cyclically pitched on both sides. By controlling pitch on both sides, the torsion in the flat plates is minimized. This design feature further allowed for the use of a thin plate of carbon fiber to minimize weight and inertial effects. The thickness of the flat plate airfoils was only 0.254 mm and has the

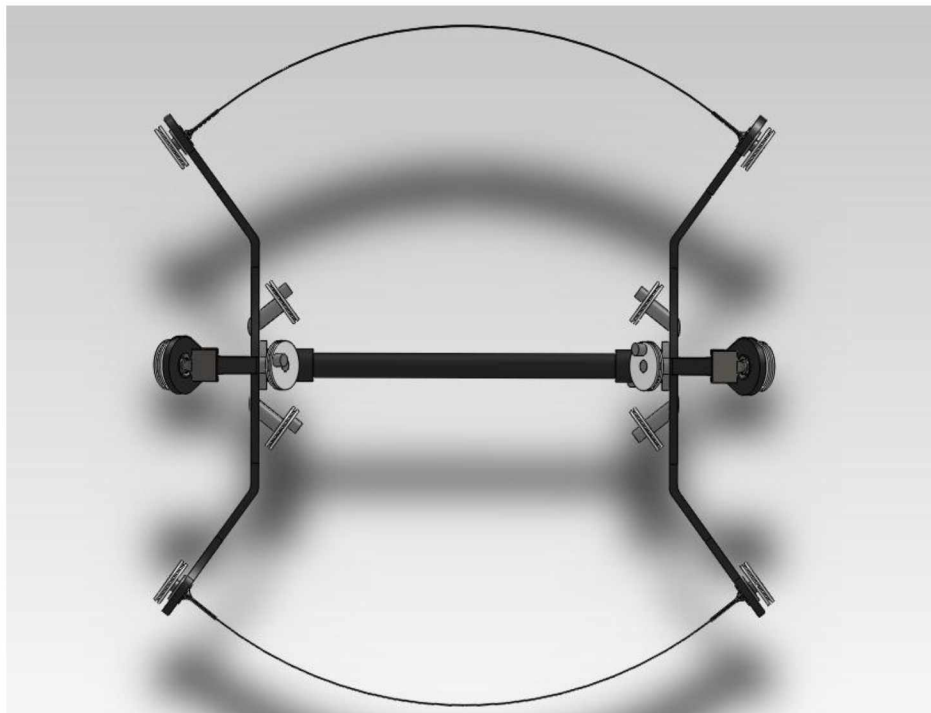


Figure 8: A SolidWorks 2011 model showing the chosen geometry of the structure supporting the airfoils with parallel oscillating pulleys for one to one pitching.

advantage of a decreased weight and had a sharp leading edge. Benedict et al. (2008) also found that a sharp leading edge generates more thrust than a blunt flat plate airfoil. An ultimate design goal was to minimize the overall weight, and specifically the weight that rotates away from the horizontal axis in order to reduce the inertial force.

3.8 Cyclic Pitching Mechanism

The design of the four armed spider supports was chosen in order to intersect the airfoils perpendicularly from a known angle of the airfoil geometry. Previous cycloidal rotor designs that have focused on being light weight have used a horizontal axis of rotation with a four bar system that is parallel. The bars are set at a constant distance from the central axis of rotation. The four bar mechanism is attached to the airfoils some distance greater than the quarter chord from the leading edge in order to achieve a cyclic pitch as the airfoils make a full revolution. This type of design was shown in Figure 5. This type of four bar mechanism would be difficult to implement for the tensile rotor. A four bar mechanism was not implemented in the design because the plane of oscillation for the airfoil at the spider connection is not perpendicular to the axis of rotation. Shown in Figure 9 are the cyclic cam pitching mechanisms that were used in place of the four bar pitching mechanisms.

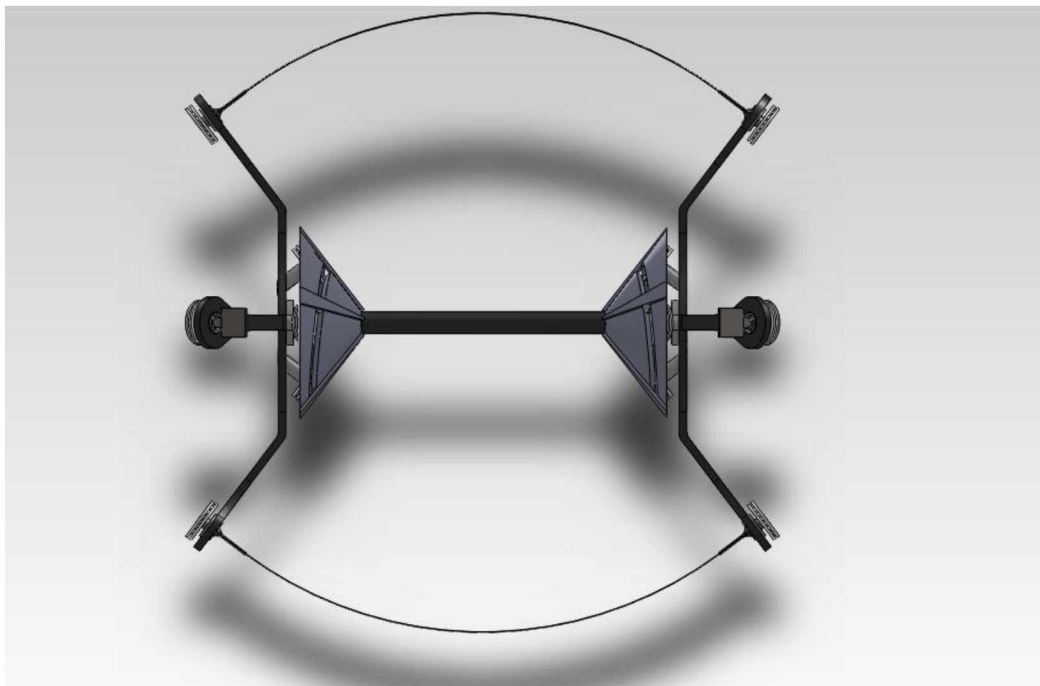


Figure 9: A cross-section view showing how the cyclic pitching mechanisms will be installed.

The geometric design of the structural spider supports further reduced weight because the pulleys are located at the base of the supports. The spider supports bent arm length was determined by the base pulleys being designed perpendicular to the

oscillating plane of the airfoils and to be driven by the spider supports. The flat plate airfoil connection to the spider supports is also cantilevered beyond the bearing locations that are mounted to the horizontal rod to act as a flywheel for stabilization. The supports were also designed to act as a re-curve bow in resisting deformation of the airfoil during rotation.

A cyclic pitching mechanism was used for each spider support. The flat plate airfoils were pitched by spectra line in tension, connected to a pulley on one end of the airfoil and then to the corresponding base pulley. As the pulley at the base of the support is pivoted $\pm 40^\circ$ with respect to the rotating spider support, the pulley rigidly attached to the airfoils will rotate with an equal angular displacement. The two pitching mechanisms are fixed on the cylindrical carbon fiber rod, acting as a stationary cam path for the pegs in the base pulleys to oscillate during rotation.

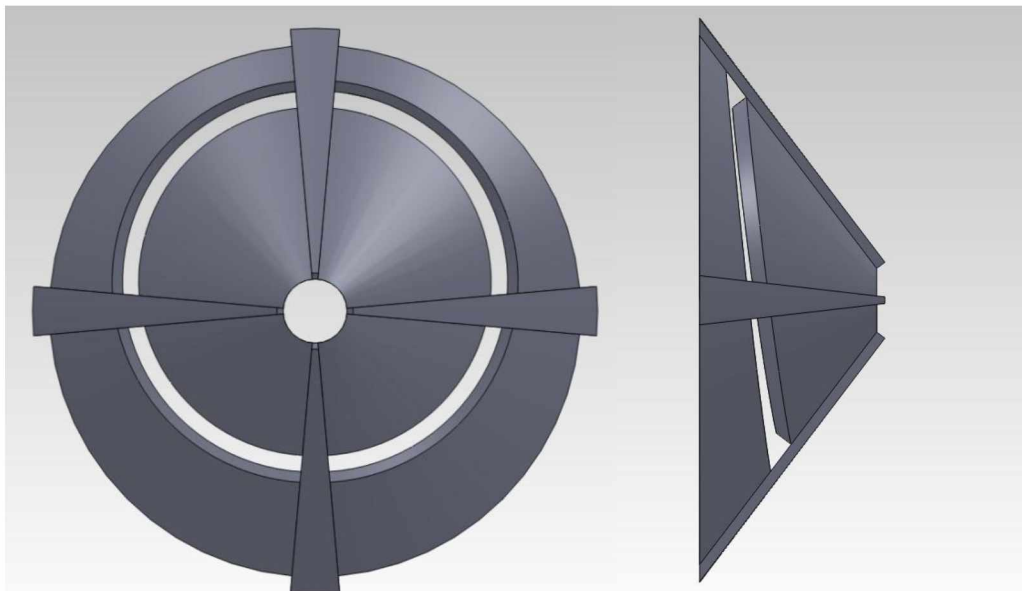


Figure 10: The cyclic pitching mechanism which represents an offset disk of an offset four bar method.

The pulleys only oscillate a total of 80° , which allowed for a part of the spectra line to be firmly fixed (glued) to the pulleys so that no slipping occurred. A V-notch in the pulleys was machined for the spectra line to have more contact area to be bonded to the pulleys.

The pitching mechanism shown in Figure 10 is a conical shell with an offset circular cam path that accommodates a free rotating oscillating peg between the pitching mechanism and the pulleys at the base of structural support. The cam path is perpendicular to the conical surface at all locations. This allows the pegs of the base pulleys to remain parallel to the plane of oscillation of the airfoils. As the pulleys are rotated, there is a small change in the distance from the axis of rotation of the pulleys

because they are cylindrical. This distance will cause the angle of attack to vary slightly from purely sinusoidal. To minimize this distance, the pulleys are small and the location of the oscillating peg that rides in the cam path is not at the edge of the pulleys for structural stability.

The cyclic cam pitching mechanism is a complex aspect to visualize for this cycloidal rotor design. It helps to look at the mechanism in two dimensions as the conical aspect is the last development that allows the pulleys at the base of the spider structural supports to oscillate parallel to the pulleys connected to the airfoils.

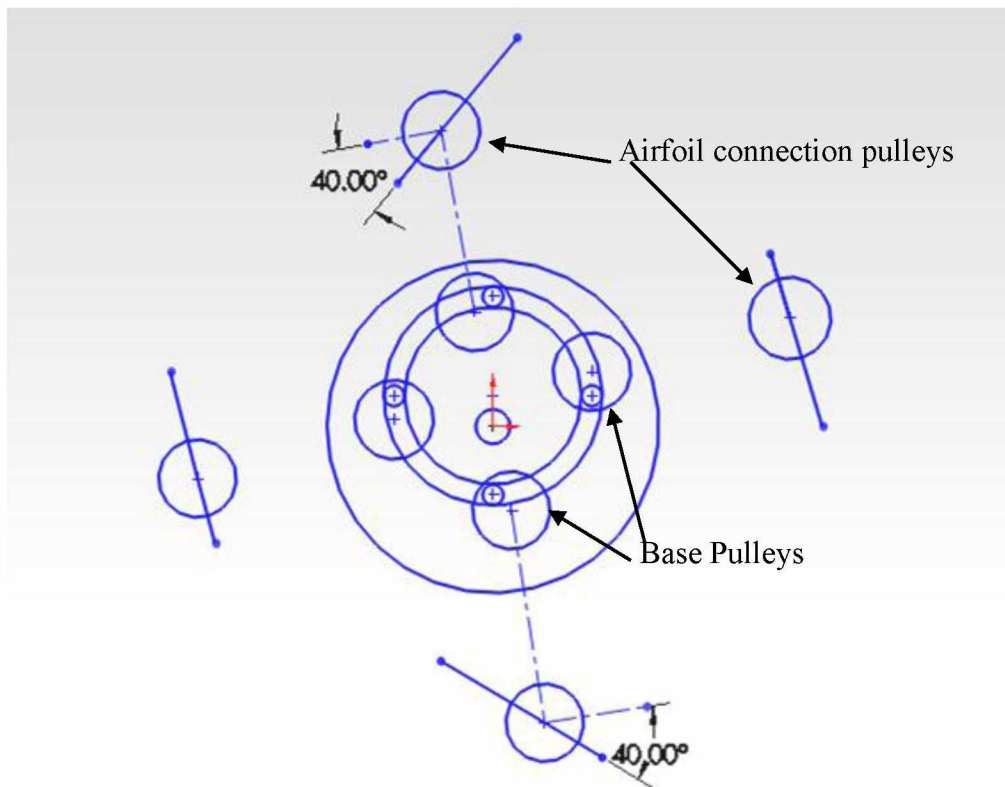


Figure 11: Two dimensional representation of the cyclic pitching mechanism. The angle of the pegs with respect to the center of the base pulleys is $\pm 40^\circ$ for the top and bottom and 0° on the side.

In Figure 11, the base of the red arrows represents the origin, and the axis of rotation comes out of the page. Starting from the top and taking a counter-clockwise rotation the oscillating pegs follow the point of rotation of the base pulleys in the cam path. The top base pulley pitches the corresponding connection pulley with a 40° increase in amplitude, pitching the trailing edge of the airfoil, represented as the line through the connection pulley, upward. The angle of the leading edge of the airfoils is the opposite of the pitched angle of the oscillating pegs because they are following the base pulleys' axis of rotation. This orientation will match the pitch shown in Figure 26.

As the top pulley rotates 90° counter-clockwise within the stationary cam path, a neutral pitch will occur. This then rotates into a negative pitch for the oscillating peg, but a positive pitch for the leading edge of the airfoil at a 180° rotation from the top of Figure 11. Then at 270° from the top, the flat plate airfoil is back to a neutral position. Making a full rotation puts the airfoil back to a negative 40° pitch with respect to the leading edge, completing one revolution of cyclic pitch. All four airfoils will be pitched in this cycle, but at a 90° phase shift from the preceding airfoil.

The dimensions of the conical pitching mechanism are calculated from the base pulley geometry. The pegs were 0.2743 cm from the center of the base pulleys. Because the pulleys oscillate $\pm 40^\circ$ the differential distance the peg travels can be calculated by 0.2743 cm multiplied by 2 times sine of 40° . Because the pulleys are always perpendicular to the cam path this differential distance was applied to the conical surface instead of the before mentioned two dimensional case. Accounting for the thickness of the peg and the location of the centers of the base pulleys fully defined the cam path.

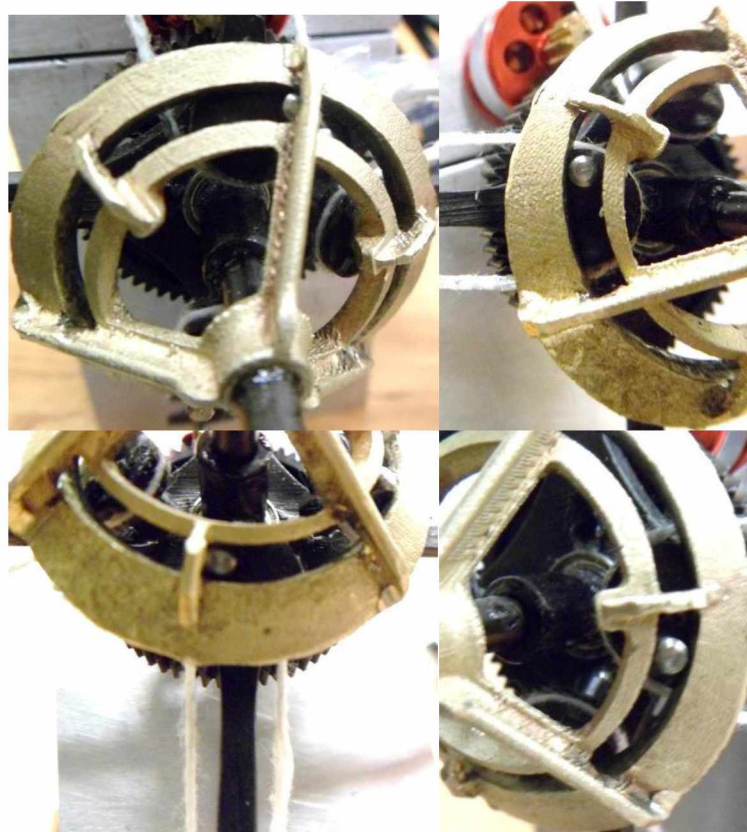


Figure 12: The pitching mechanism with the base pulleys and oscillating pegs are shown in cyclic pitching.

Figure 12 shows the pitching mechanism with a base pulley making a full revolution to demonstrate the oscillation of the peg. At the top left the peg receives a positive 40° pitch, the top right a neutral pitch, the bottom left a negative 40° , and the bottom right a neutral pitch. From the bottom right the pulley would then end at the top left of Figure 12 completing a full revolution.

3.9 Design of the Entire Rotor

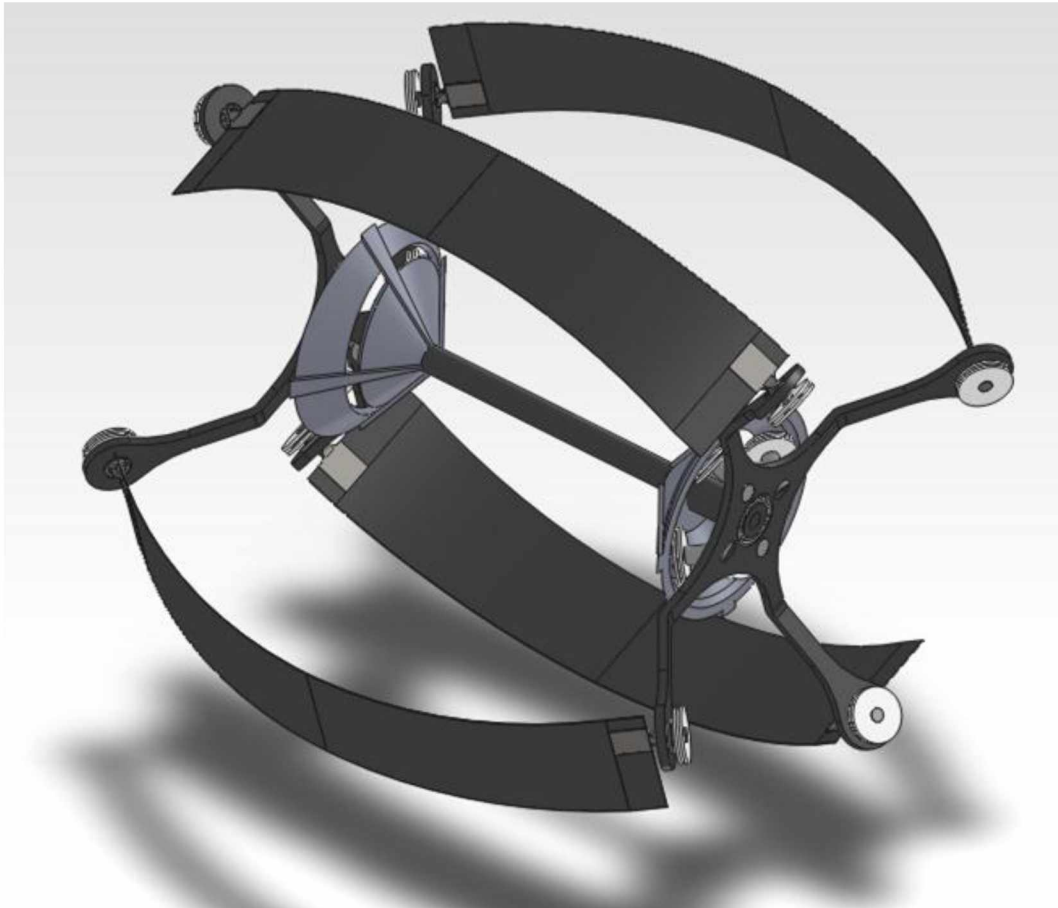


Figure 13: SolidWorks 2011 full design model.

The airfoils, center rod, and spider supports in Figure 13 were made of unidirectional pre-impregnated carbon fiber. The unidirectional pre-impregnated carbon fiber tape has an exceptional tensile capacity of 1903 MPa. The structural supports were constructed of 12 layers of alternating unidirectional carbon fiber, for a total thickness of 1.5875 mm. The pulleys are shown in white to be distinguishable from the carbon fiber, but were made from black acetal rod. The base pulleys are connected to the connection pulleys using spectra line, but are not shown in Figure 13. The center rod extends towards the left of Figure 12 and is connected to a fixture for testing. A spur gear was mounted to the left spider support to gear down the motor with an 11 tooth pinion gear, resulting in a gear ratio of 5.64. For a top speed of about 2500 RPM, the maximum motor efficiency occurs at 2217 RPM.

One potential drawback to this design is that the airfoils are curved, forcing air in the axial direction instead of just the vertical direction. This causes two opposing axial air flows that could lead to a lower efficiency.

4 Structural Analysis

4.1 SolidWorks Simulation

SolidWorks Simulation was used to determine the stresses and displacements of the main components of the rotor. A major goal of the project was to design the rotor to be as rigid as possible and experience minimal deformation. This Von Mises stress analysis confirmed that the structure of the cycloidal rotor was sufficient to withstand the predicted forces that would be placed upon it during testing.

4.1.1 Airfoil Stress/Displacement

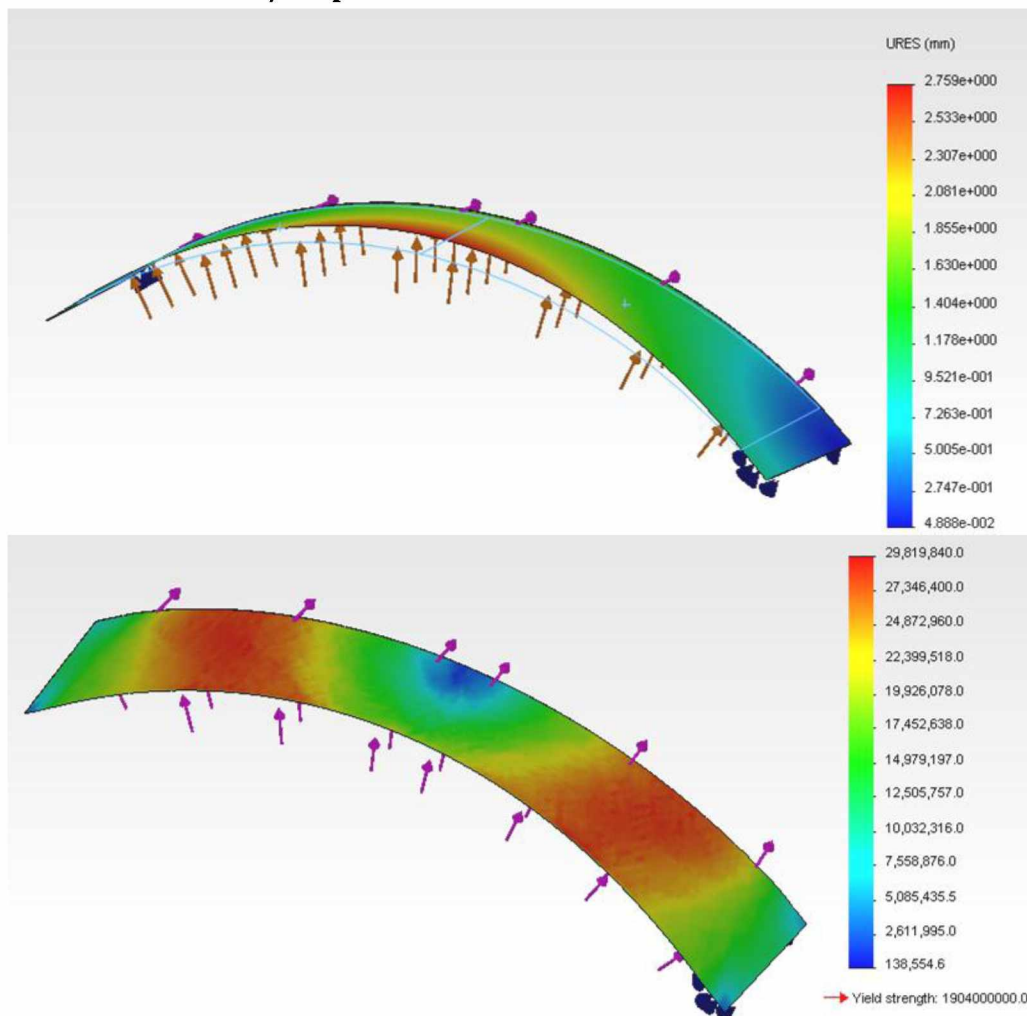


Figure 14: Plots of the displacement (top) and Von Mises stress (bottom) under a uniform load (purple arrows) that represents the thrust force during rotation. The displacement shown exaggerated for better visualization. Maximum displacement is 2.8 mm near the center (red).

Figure 14 shows a stress simulation with elastic restraints (represented by blue cones) and the airfoil deformed as would be expected when a distributed normal force is applied. The normal force represented the thrust of the rotor and the ideal displacement of the airfoils was symmetrical. The load is distributed and is 453.59

grams for thrust and 226.8 grams for drag. The maximum expected thrust produced by the entire rotor during actual operation is only 150 grams created by both airfoils. The testing load is over three times the expected value and is applied to a single airfoil for an added factor of safety. This safety factor will also account for the inertial force that will be supplied to the airfoils because of the high rotational speeds reaching 2500 RPM.

Analysis of the displacement due to these forces showed a large displacement of up to three millimeters, but this is for an extreme case of 453.59 grams thrust and 226.8 grams of drag. A thrust of 157.2 grams gave a displacement of 1 mm and will be constrained by an even smaller deformation from the structural supports under normal operation. The Von Mises stress shown in the bottom of Figure 14 indicated that the airfoil will only experience 1.6% of the yield stress under these conditions.

4.1.2 Structural Support Stress/Displacement

Figure 15 shows the displacement that results when a pressure of 6895 Pascals/arm is applied on the spider supports. This simulation was performed in order to evaluate the structural integrity during operation. The results indicate that the stress experienced (not shown) is only about 1% of the yield stress, and the maximum displacement was only 0.1278 mm at the edge of the arm.

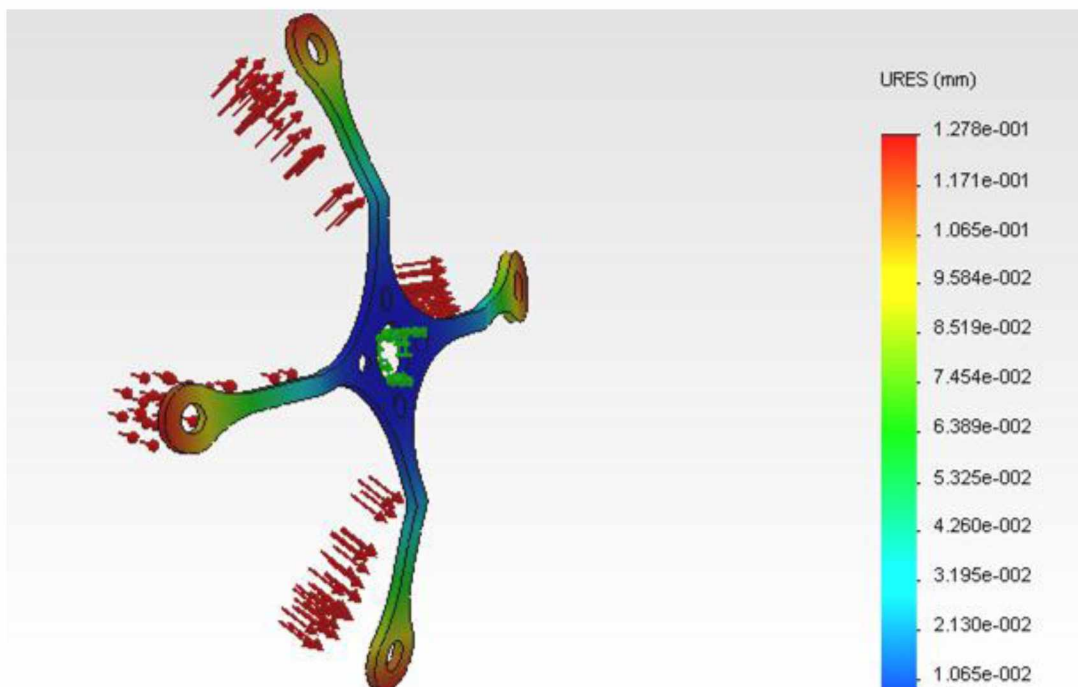


Figure 15: Displacement of the spider structural support under equal loading on all four arms. Maximum displacement occurs on the edge of the arm and is 0.1278 mm.

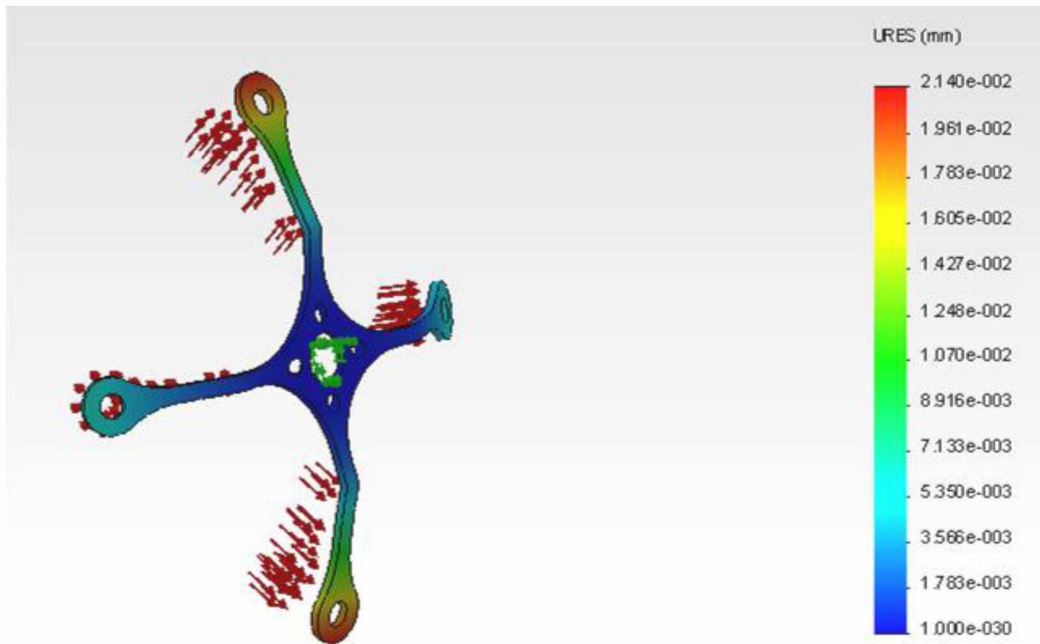


Figure 16: Structural Support with loading that is more realistic with two of the arms attached to the airfoils with ± 40 degrees with more load due to drag and, thrust than the non-pitched airfoil arms.

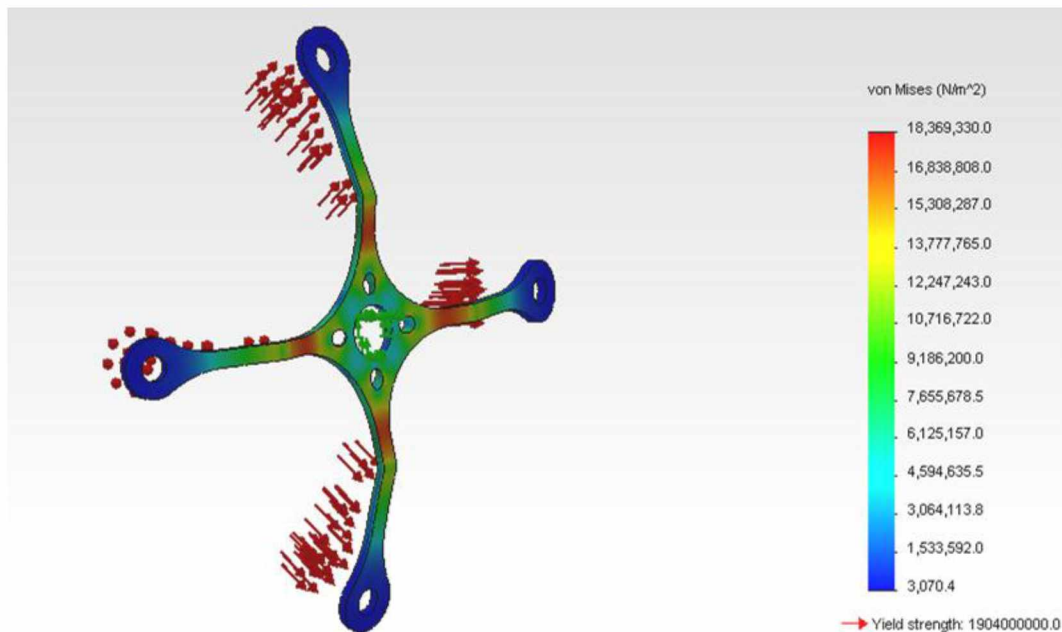


Figure 17: Stress in the structural supports under larger than necessary conditions.

Figure 16 shows the spider arms with expected loading conditions. The top and bottom arms had a 226.8 gram load from aerodynamic and inertial forces, where pitching would occur with a deformation of just 0.00214 mm. The two structural arms on the sides were subjected to a smaller load to simulate only the inertial force with no pitch. A centripetal acceleration ($a_c = \frac{U^2}{r}$) of 2800 m/s² for an RPM of

2000 was calculated given the radius of rotation, r , and the velocity U . With an expected mass of no more than 4 grams/arm the force is 11.2 N. A load of 113 grams was placed on the arms for a factor of safety and to demonstrate that a minimal deflection of 0.002 mm is simulated.

Figure 17 shows the stress experienced by the structural supports was less than 1% of the expected yield stress when the maximum load was applied to all of the structural arms. A fatigue analysis shown in Figure 18 was performed with varying loads on the structural spider supports, airfoils, and center rod to estimate the life expectancy of the rotor. Areas shown in blue indicate that there were no points of failure within the entire structure for a cyclic loading of 8 billion cycles.

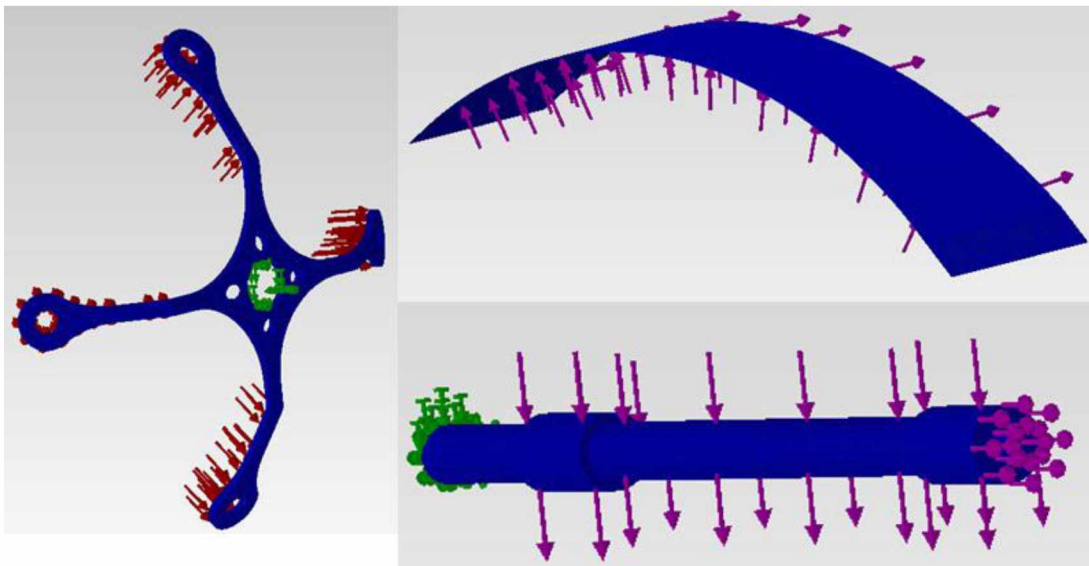


Figure 18: Fatigue analysis of increased loads on the main components of the rotor.

5 Rotor Prototyping and Manufacture

5.1 Spider Support Compression Molds

The spider supports were made using compression molds. The molds consisted of a two dimensional profile of the supports with a machined bending jig to bend the spider arms. An aluminum spacer plate of 1.5875 mm thickness was placed between the two molds and bent to the desired angle of 37.15° from the vertical axis. The spacer of aluminum was used to create the desired thickness that would eventually accommodate the carbon fiber supports during manufacturing.

Compression molds were utilized to create the spider supports that maintain the airfoils a fixed distance away from the axis of rotation about the x-axis. This type of mold was used so that the supports will be smooth on all surfaces to minimize any structural issues that could lead to failure. The compression molds also allowed the use of pre-impregnated carbon fiber commonly referred to as prepreg, which is carbon fiber that is already immersed in a matrix of thermosetting resin. The advantage of the thermosetting resin is that a high strength material can be obtained by using a high temperature programmable furnace. Ramping the furnace temperature during setting allowed for a more rigid resin and higher strength material, but in turn reduced ductility. However, if the part is designed to experience only small deflections this tradeoff is not a concern.

Figure 19 shows two views of how the compression molds are assembled without the carbon fiber. On the left is a view that shows holes that were used to drill into the carbon fiber supports to mount the base pulleys. The view on the right shows the displacement pins that maintained constant thickness between the compression molds.



Figure 19: Compression molds shown with pegs and center location hole as well as an angled hole for pulley support drilling.

The CNC program used to manufacture the compression molds is listed in Appendix 5.A and was written using a simple text editor for ease of use with the vertical milling machine controller. The G-code shown in the appendix lists X, and Y location with R denoting the radius definitions to create the two dimensional profiles of the compression molds. The program used a 9.525 millimeter end mill to cut a

roughing and finish pass in a fixture plate to allow for chip clearing. The holes for the displacement pins and center hole were pre-drilled on a manual mill. The blank of aluminum was then bolted down to the fixture using the predrilled holes. The two different sized molds were placed side by side and cut in one program with a roughing pass. A final finishing pass of 0.254 millimeters was then cut for a smooth and accurate finish of the molds.

5.1.1 Material

The material chosen for the molds was high temperature treated aluminum for its low thermal expansion and therefore minimal change of geometry during the curing process of the resin. Aluminum is more easily machined than steel and is a typical material choice for compression molds.

5.1.2 Bending Jig

Figure 20 shows the bending jig tool used to bend the arms of spider supports. It is a male and female machined die set. The jig angle is slightly greater than the angle designed for the spider supports to account for spring back of the aluminum. The spring back occurs because of the aluminum's elastic response after the pressure from the hydraulic press has been released after bending. The spring back of the material is not an easy property to quantitatively predict and is best determined by testing. The degree of spring back depend can on a variety of material properties and geometry. Precision angle blocks were utilized in a vertical milling machine to orient the jig in



Figure 20: Bending jig used to create specified angles in the spider support compression molds.

the mill vice for accurate machining. Two symmetrical cuts were made at 20° from the horizontal to create an angle in the female section of the die set of 140° . As the

actual angle had yet to be determined, it was then tested and indeed produced an angle very close to the 37.15° angle required. The 20° angle that was used was recommended by a very experienced machinist who was familiar with the aluminum being used.

5.1.3 Spider Arm Dimension

The spider support arm molds were not the same dimension because of the finite thickness of the intervening material during the bending process. Figure 21 shows a difference in the radius of curvature between the inner and outer mold forms, which causes an uneven length in the arms. The determination of the additional length the outer form required to be aligned is a complex issue, and one an entire industry of



Figure 21: Test specimen of two 3.175 mm heat treated aluminum with 1.5875 mm in the middle where the carbon fiber arms will be determining the differential length needed in the arms.

metal bending has been built upon. The geometry after bending depends on the material properties as well as initial geometry and cross-sectional area of the location of bending. In Figure 21, one end of the test specimen is riveted to represent an arm for the spider support molds. The difference in length between the center piece of aluminum and the two forms is equal. The difference in length is added to the outer form and subtracted from the inner form before bending. This allowed the inner and outer mold arms to be aligned after bending.

5.1.4 Displacement Pins

The pins of 2.38125 mm diameter were designed to equal the inner diameter of the bearings. They were placed in the outer compression mold arms and had multiple functions. They created accurate dimensions in the carbon fiber spider supports and kept the holes for bearing placement aligned from the axis of rotation. A tight fit for the bearings was also achieved in the carbon fiber spider support. The pins also acted as a means to stop the carbon fiber from being compressed beyond the thickness of 1.5875 mm. Without the pins the blued steel spring clips used to hold the mold forms together would have over compressed the spider arms while the resin set in the furnace. A through pin was also placed in the center of the spider supports mold to insure the centers of the spider supports were located in the carbon fiber.

5.2 Airfoil Compression Molds

The airfoil compression molds were made of the same tempered aluminum and required a slightly different approach than the spider compression molds. The cylindrical bending of the flat plate airfoil molds occurred before the tapered profile of the airfoils was machined into the inner and outer forms. This approach was taken because any deviation in width of the aluminum would result in a non-cylindrical bend because of higher stress concentration in the narrowest location. Similar to the construction of the spider supports, the outer form was longer than the inner form due to curvature in the part. The amount of spring back in cylindrical bending was much greater than the spring back that occurred from point bending. A much longer length was ultimately needed was cylindrically bent, with one end anchored to a cylinder of appropriate diameter while the other end was used to torque around the cylinder. The longer torque arm reduced the necessary force, which allowed more precise bending.

5.3 Programmable Furnace

A Thermolyne programmable furnace was used with a temperature bandwidth of $\pm 3^{\circ}\text{C}$. The furnace program was written to meet the manufacturer's recommendation for the thermosetting resin. The program was a ramping function of $3.3^{\circ}\text{C}/\text{min}$ until 93°C was reached, held for 20 minutes to allow any air bubbles to escape before ramping to 135°C to set the resin. The temperature was then held for one hour before cooling back down to 120°C and removed from the furnace.

5.4 Cyclic Pitching Mechanism

The pitching mechanisms were originally designed to be machined from Delrin, which has a good strength to weight ratio and sliding properties for the cam path. However, machining a conical shell of irregular angle with a perpendicular cam path to the surface of that cone was not feasible without a 5-axis milling machine. A 5-axis milling machine was not available, so a different approach using bronze was selected that compromised the overall weight reduction of the rotor. Each pitching



Figure 22: Sprue tree with lost wax casting bronze pitching mechanism.

mechanism of bronze had a mass of 15 grams. Lost wax casting was utilized to create the pitching mechanisms. The Thermojet Wax Printer used to create the molds is accurate to within 0.05 millimeters and captured the fine details necessary to create a reliable cam path. The wax used was specially designed to burn away as a mold of the wax print. Before the mold is made sprues are attached to the wax print. Sprues are wax cylinders that when burned out of the mold allow for the 1200°C liquid bronze to be forced into the mold, ultimately leaving behind a bronze copy of the pitching mechanism. Figure 22 on the left shows a sprue tree of bronze used as a path to create the pitching mechanism shown in the right of the figure. The mechanism was then cut off of the sprue tree and the cam path refined for operation.

5.5 Hardware



Figure 23: Additional hardware used for the pulley mechanism, showing a progression of assembly from right to left.

Figure 23 shows some of the more conventional components, such as connecting rods, pulleys and oscillating pegs. The base pulleys were machined of Delrin, which has a high compressive strength to weight ratio and rotates easily on the steel rods that connect them to the carbon fiber spider supports. The pulleys that are attached to the



Figure 24: Carbon fiber spider supports with bearings inserted.

airfoils are fixed rigidly with epoxy that withstands the torque placed on the pulleys. The rods attached to all of the pulleys and the oscillating pegs are made out of precision steel 2.381 millimeters in diameter. This diameter allowed for a press fit into the bearings. The precision finish on all of the oscillating shaft small part items reduced machining time.

5.6 Spider Supports, Airfoils, and Final Assembly

Special care must be taken when machining carbon fiber. The particles are small enough to be lodged in the lungs and proper precautions should include, but are not limited to, eye protection, use of a ventilation mask, and a powerful vacuum to minimize airborne particles.

Figure 24 shows the carbon fiber spider supports with the bearings installed. The supports are created with opposing unidirectional layers at the center of the supports. The layers alternate 90° from each other in the center of the spider supports; while the arms remain unidirectional for every layer. This leaves the arms in tension as the perpendicular layers overlap only in the center of the spiders for structural integrity. The average thickness for each layer is 0.14 mm, and twelve layers were used to achieve the desired thickness of 1.59 mm. The compression molds were used as a template while using a Dremel sanding drum to machine the carbon fiber spider supports. The structural spider supports weighed four grams a piece with the bearings installed.

The flat plate airfoils shown in Figure 25 are also made from unidirectional carbon fiber and are very thin. Each airfoil is made from only two layers of carbon fiber, yet can withstand the torque that the cycloidal rotor required to rotate without angular lag between the spider supports.

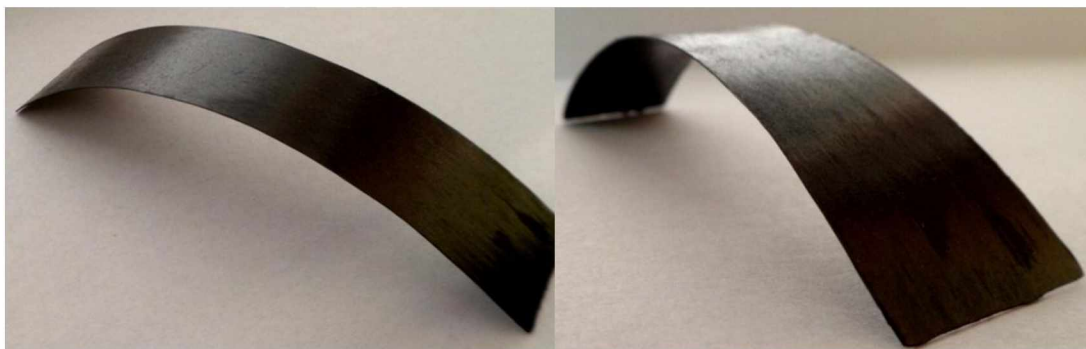


Figure 25: Two views of the carbon fiber airfoil geometry.

In previous cycloidal rotor designs, torsion in the airfoils has been an issue because the rotor was driven on only one side of the rotor. The rotor had to transmit all necessary power to the other through the airfoils. This required the airfoils to be reinforced and sufficiently rigid to maintain efficiency, but led to heavier airfoils that required more structural support.

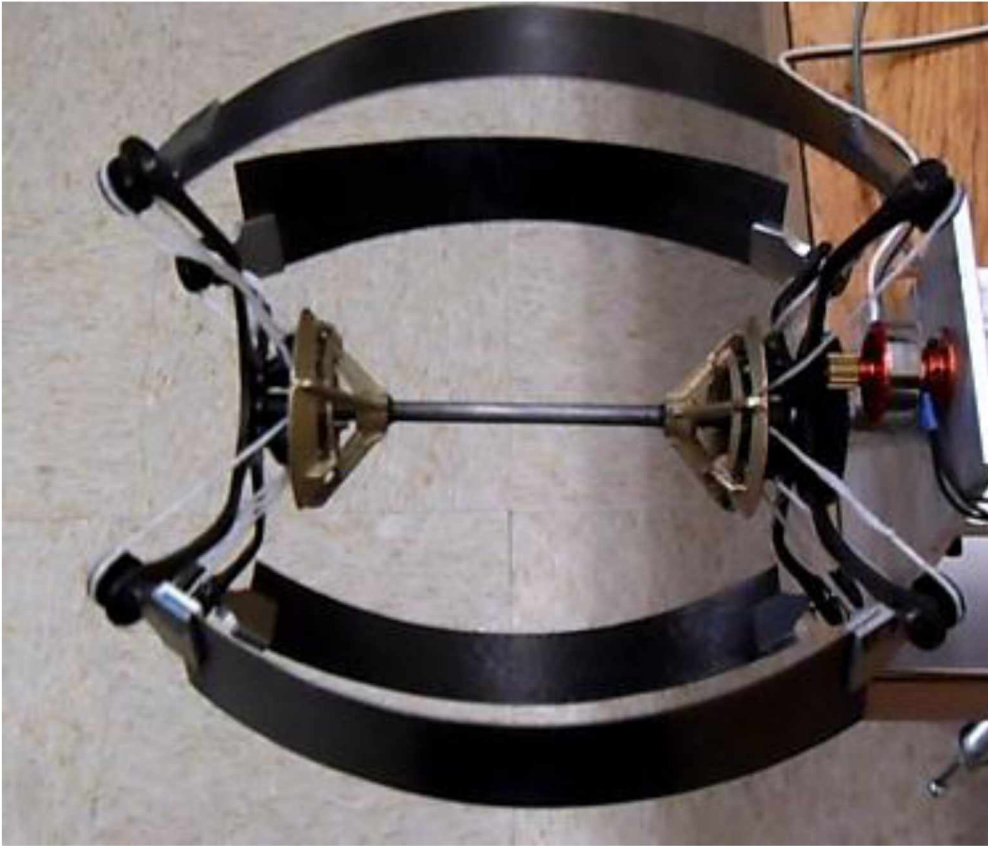


Figure 26: The final completed assembly with the rotor mounted to the test stand and meshed with the motor's pinion gear.



Figure 27: Demonstrating the pitching of the airfoils to the designed $\pm 40^\circ$.

Figure 26 shows the final assembly of the cycloidal rotor. Pitching the airfoils on both sides of this rotor is believed to permit the airfoils to be thin and flat to reduce weight while still being able to transmit torque to the free end of the rotor without angular lag of the spider supports.

Figure 27 shows the pitching with the top airfoil pitching downward and the bottom airfoil pitching upward with respect to the leading edge. The airfoil in the top of Figure 27 shows an inconsistent angle of attack along the span. This can be seen by comparing the angle (relative to the horizontal) of the middle and edge of the airfoil at the connection to the spider support. These two are not exactly parallel. This demonstrated that there is some torsion occurring in the airfoil on the free end as well as on the other side of the cycloidal rotor.

The rotor was assembled with an amount of pretension in the airfoils so that the rotor was able to spin without angular delay between the spider supports. This also accounted for any slack that might have been present at lower RPM when inertial forces are smaller.

The motor is mounted in a test stand for bench testing and is meshed with the spur gear to allow for smooth meshing with no resistance with the pinion gear. The pulleys are all put into place and attached using spectra kite line and the cast pitching mechanisms were aligned.

5.7 Motor, Controller, and Speed Control

The motor was chosen to operate with greater initial torque while using as little power as possible. The motor operated at a constant 11.1 volts for higher low end torque to start the cycloidal rotor. The controller consisted of a throttle that required start initiation for no false starts of the rotor while power was applied. The other electronic component was a speed controller that allowed for accurate output of constant voltage and soft start up and stopping. This eliminated jerk that would have put unnecessary strain on the rotor. Specifications can be found in Appendix 5.B.

6 Experimental Testing

6.1 Apparatus

The rotor was only tested in what is referred to as a hover test. A hover test placed the cycloidal rotor in a test stand and was secured to a solid bench. The electrical current is increased to increase the power and revolutions per minute of the rotor. The thrust was assumed to be equal to the vertical force on the rotor, which



Figure 28: Spinning cycloidal rotor to perform force and power testing.

results from a pressure differential causing airflow through the rotor. In Figure 28, it is evident that the pitch mechanisms (bronze components) do not rotate, while pitching the flat plate airfoils. To fly or hover unassisted would require at least two rotors and a way to counteract the torque produced by the two rotors by using a tail rotor similar to that of a helicopter. There could also be four separate rotors, two rotors rotating counterclockwise and the other two clockwise, which would not require any torque counteraction.

Two strain gages were mounted on the center support rod between the spur gear and the test stand to measure the thrust and axial force being produced by the rotor. The gages were placed perpendicular to measure the two forces, which were assumed to be perpendicular to each other. The gages were connected to a National Instruments DAQ 9219 system in two separate quarter-bridge arrangements to measure the resistance changes in the strain gages. The gage factor of each was 2.02. A simple static calibration test was performed to determine if the gages measured the

specified forces as intended. A load of 226.8 grams applied on the free end of the rotor, which resulted in a strain of 520 $\mu\epsilon$. It will later be shown in Section 7.1 that a SolidWorks analysis would predict a corresponding strain of 522.6 $\mu\epsilon$ for a 443.59 gram load. This is a 0.5% difference. The simulation load assumed a distributed load along the length of the center rod. The strain is assumed to vary by a linear function proportionate to the length. The experimental load on the free end is half of the simulation load because the free end of the rotor is twice the distance from the test stand. When this load was applied vertically, the horizontal gage read only 10 $\mu\epsilon$, confirming that the gages operated as expected. The expected strain values assumed that the rod is behaving as a simple cantilevered beam.

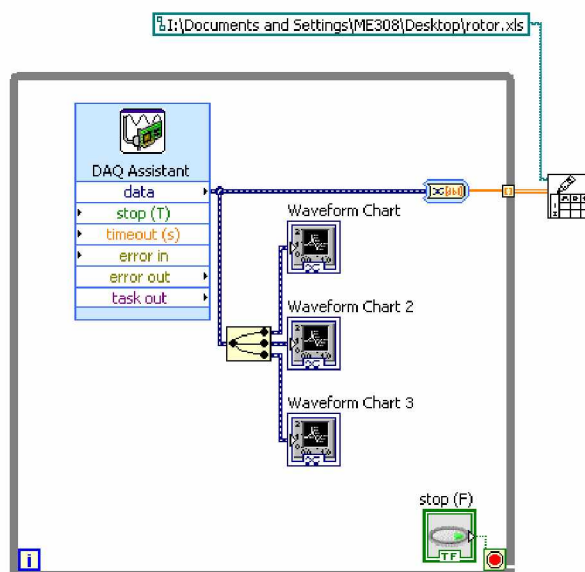


Figure 29: LabVIEW block diagram for acquiring and storing the strain data as a function of time while testing the rotor.

The LabVIEW NI DAQ assistant node shown in Figure 29 allowed for easy communication and signal interpretation because it measures the voltage signals and interprets them based on the gage resistance and gage factor into strain values.

6.2 Pitch Mechanism Test

The electric current was determined by measuring a voltage drop across a fixed length of 18 gauge wire of known material properties. The speed controller used between the battery and the motor maintained a constant 11.1 volts from the battery. To increase power and the RPM of the rotor, the electric current is increased. The resistance of the wire is the resistivity, ρ , multiplied by the ratio of length to area.

$$R_{wire} = \frac{\rho L}{A} = 1.72 \times 10^{-8} \Omega m * \frac{0.2667 m}{8 \times 10^{-8} m^2} = 0.0057341 \Omega$$

For example at 2200 RPM with only one the pitch mechanism engaged the electrical current can be calculated using Ohm's Law, where voltage, V , is equal to the electric current, I , multiplied by the resistance, R :

$$I = \frac{V_{drop}}{R_{wire}} = \frac{0.00632V}{0.0057341\Omega} = 1.10218 \text{ Amps}$$

This required a power of 12.23 w, and without the mechanism engaged a power of 9.623 w was required just to spin the spider support at 2200 RPM. This left 2.611 w per pitching mechanism for a total of 5.222 w at this RPM.

6.3 Total Power and Strain Testing

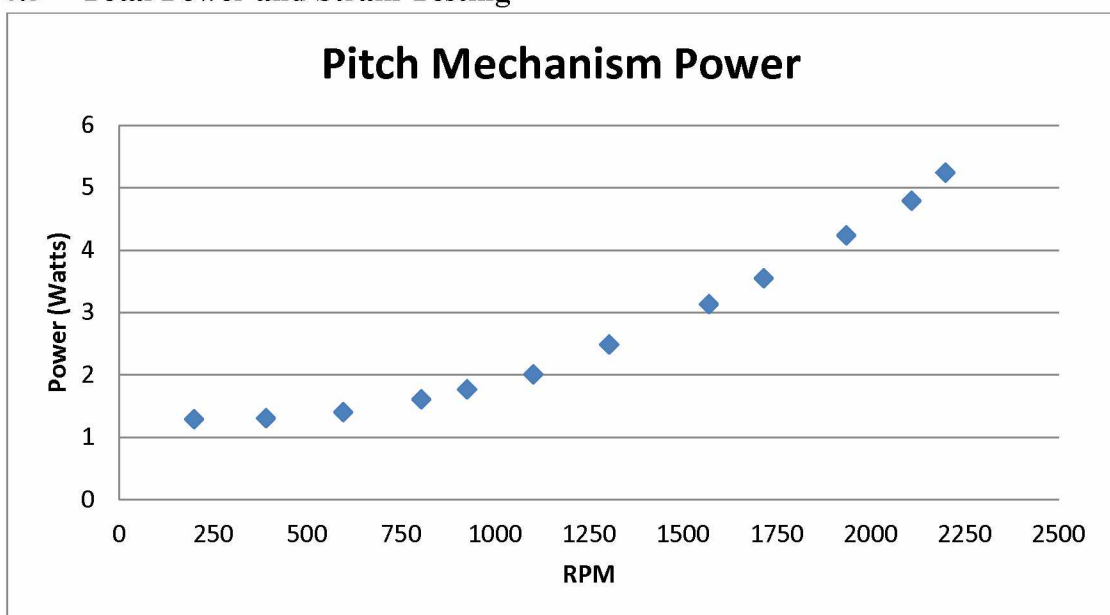


Figure 30: Plot showing experimental power consumed by both pitching mechanisms as a function of RPM.

The mechanical pitch power shown in Figure 30 was found to be 13% of the overall power consumed when compared to the total power measured for an operating RPM of 2200. The power components of rotorcraft are proportional by the cube of the RPM; however the pitch mechanism is not. The data would be characteristic of the cubed relationship if the power intercept were zero and varied with a linear relationship when plotted.

Figure 31 shows the pitching power plotted against the cube of the RPM. Absorbed power from the pitch mechanisms could be attributed to friction. It is thought that as the rotor increases in speed the coefficient of friction decreases within the cam path. Power lost to friction also decreased as the rotor approached operating speeds.

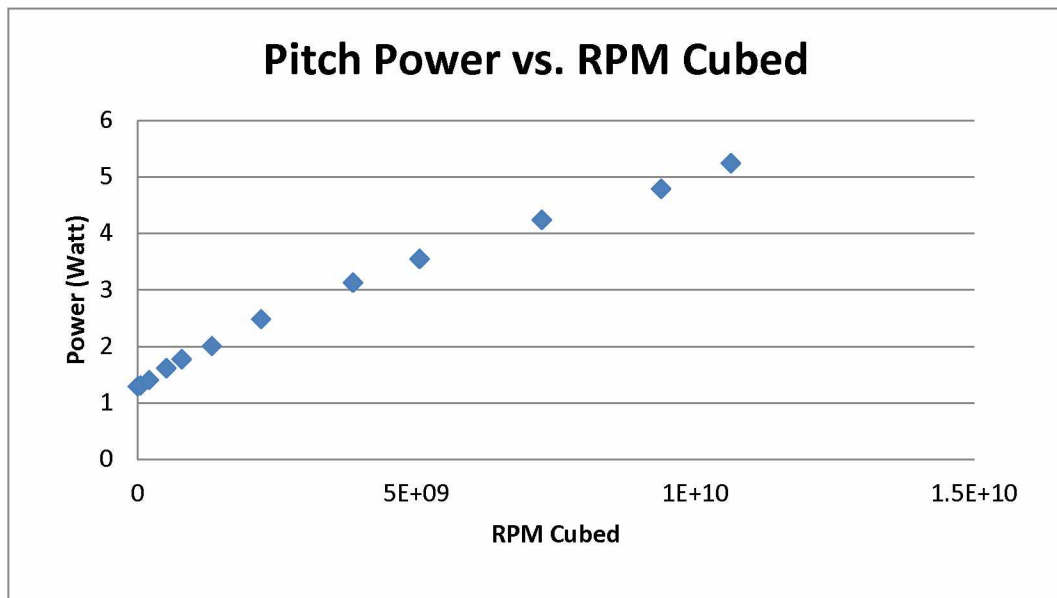


Figure 31: The pitching mechanism power versus the cube of the RPM with an R^2 correlation of 0.9874.

Once the mechanical power was determined for the rotor, the airfoils were attached and the voltage drop across the 18 gauge wire was again used to determine the electric current. The strain was simultaneously measured along with the RPM. A photo tachometer measured the RPM by attaching a reflective piece of tape on one of the structural spider arms. To ensure that the tachometer was not measuring the other spider arms the RPM was measured at constant throttle of the remote control with two pieces of reflective tape on two arms, and the RPM was doubled. This demonstrated that the photo tachometer was only reading the revolutions of the arm that had the reflective tape attached.

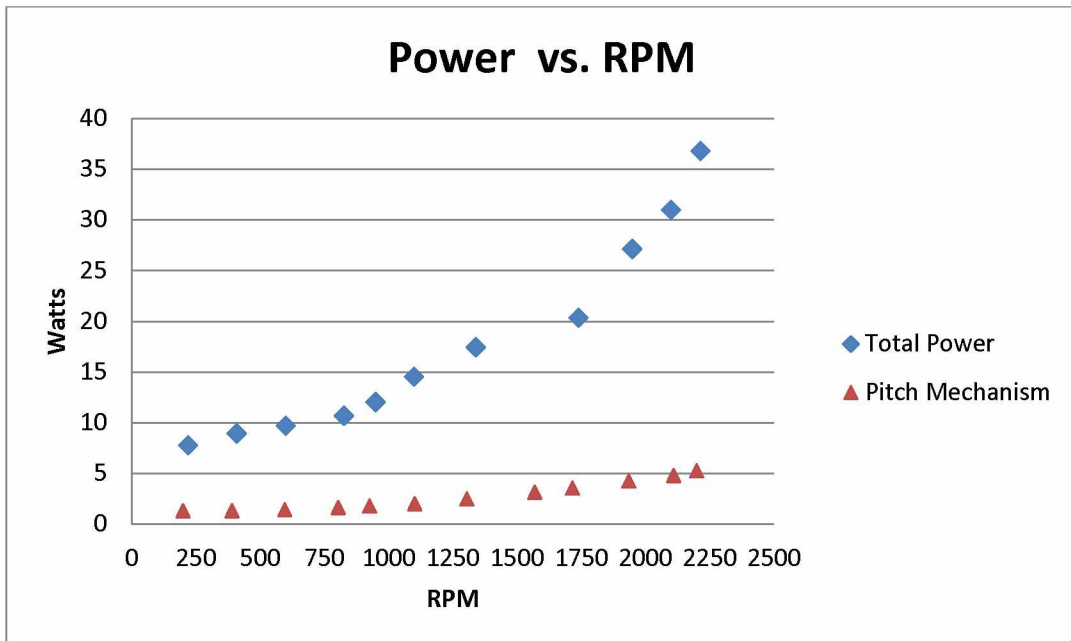


Figure 32: Plot showing the power as a function of RPM for the entire rotor assembly compared to that of just the pitching mechanisms.

Testing was not performed at RPM values above the peak efficiency of the motor due to vibration in the system, possibly caused by an imbalance in the rotor. The gearing of the motor placed the peak efficiency of the rotor at 2217 RPM. Figure 32 shows the difference between the total power and the pitching mechanism power; the difference is considered to be the aerodynamic power. This is the power required to pitch the airfoils without mechanical considerations.

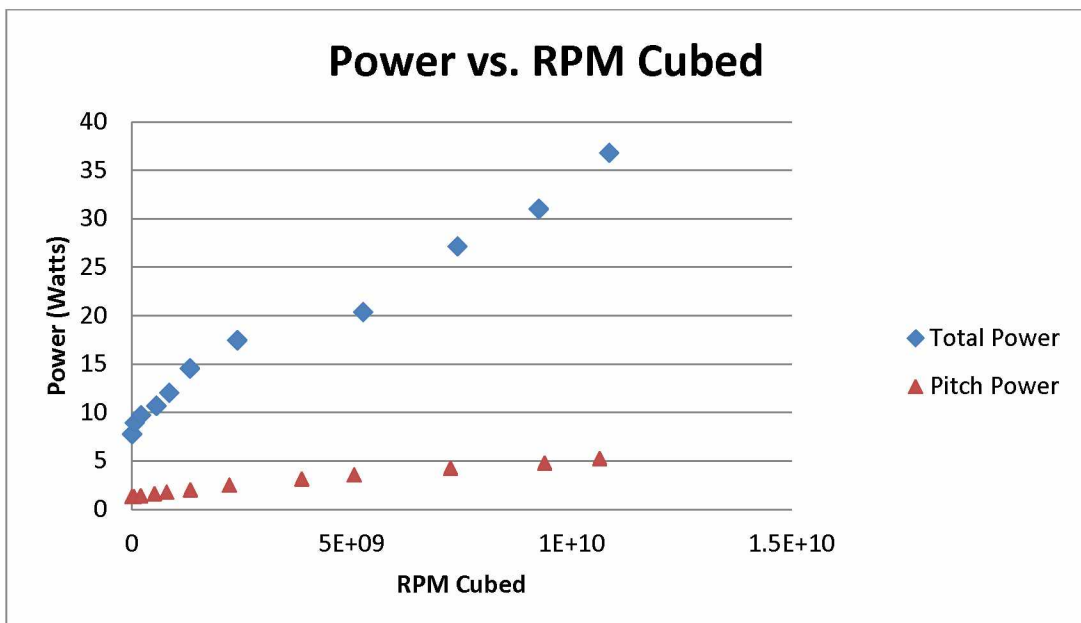


Figure 33: Plot of the relationship of the total power (R^2 correlation of 0.9821) and the pitch mechanism power (R^2 correlation of 0.9874) versus the cube of the RPM.

Figure 33 shows the total power and the pitching mechanism power as a function of the RPM cubed. Ideally, both should have a power axis intercept when plotted with the cube of the RPM. The total power near the intercept absorbed six times the power that might be attributed to friction from the pitching mechanisms. There seemed to be a discontinuity in slope between the first seven and last four data points for the total power. This artifact may be due to an increase in power loss at lower RPM.

Figure 34 shows the measured strain for both the radial and axial force measured on the center rod. Recall that it is assumed that one force does not affect the other, based on the observation that a vertical force applied on the free end resulted in a negligible strain in the perpendicular strain gage (see Section 6.1).

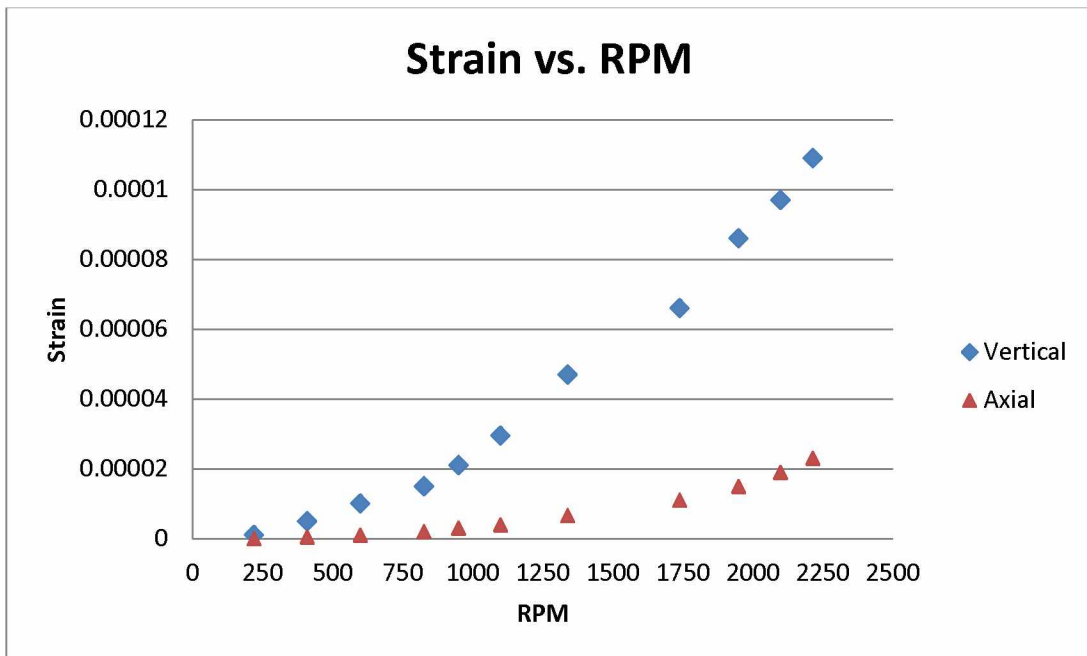


Figure 34: The measured strain values for the axial and radial directions for variable RPM.

7 Results and Discussion

7.1 Thrust and Axial Force

Finite Element Analysis software in SolidWorks was utilized to determine the strain that would be measured for a given force. In the analysis, the force was equally distributed along the rod as an approximation of the average loading that would be perceived on the rotor during operation.

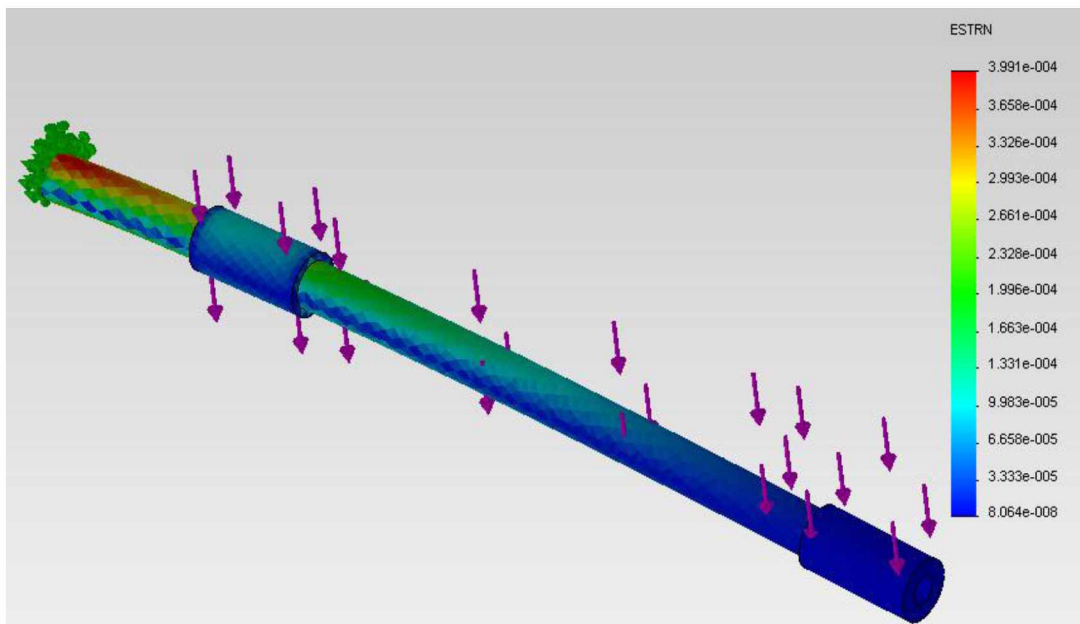


Figure 35: SolidWorks strain analysis of vertical distributed load on the rod.

A strain of $4\ \mu\text{m}$ was simulated with an applied load of 453.6 grams. A 226.8 gram load on the end of the rod yielded similar results as the simulation. This supported the assumption of a distributed load along the center rod.

Figure 35 shows a vertical load applied to the center rod with the strain on the right. A load from zero to 907.18 grams was applied in the simulation to view the strain in a wide range. This demonstrated that an increase in load on the rod created a linear change in strain. An axial force was included in this analysis for the same range of vertical force. This axial force was varied to determine how the vertical strain was affected. When an equal vertical and axial force of 90.72 grams was analyzed the axial force only changed the vertical strain by 3.2%. This supported the experimental strain results where it was observed that the axial force would not greatly influence the vertical strain, and vice versa.

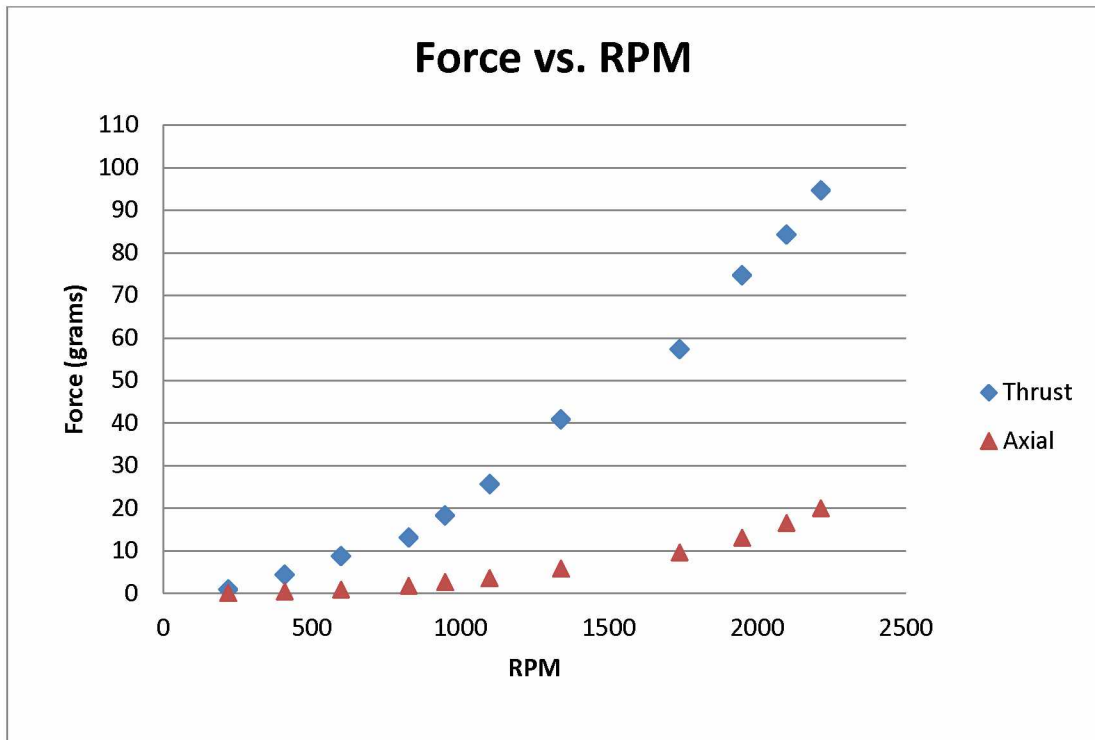


Figure 36: Plot showing the radial (thrust) and axial forces on the cycloidal rotor as a function of RPM.

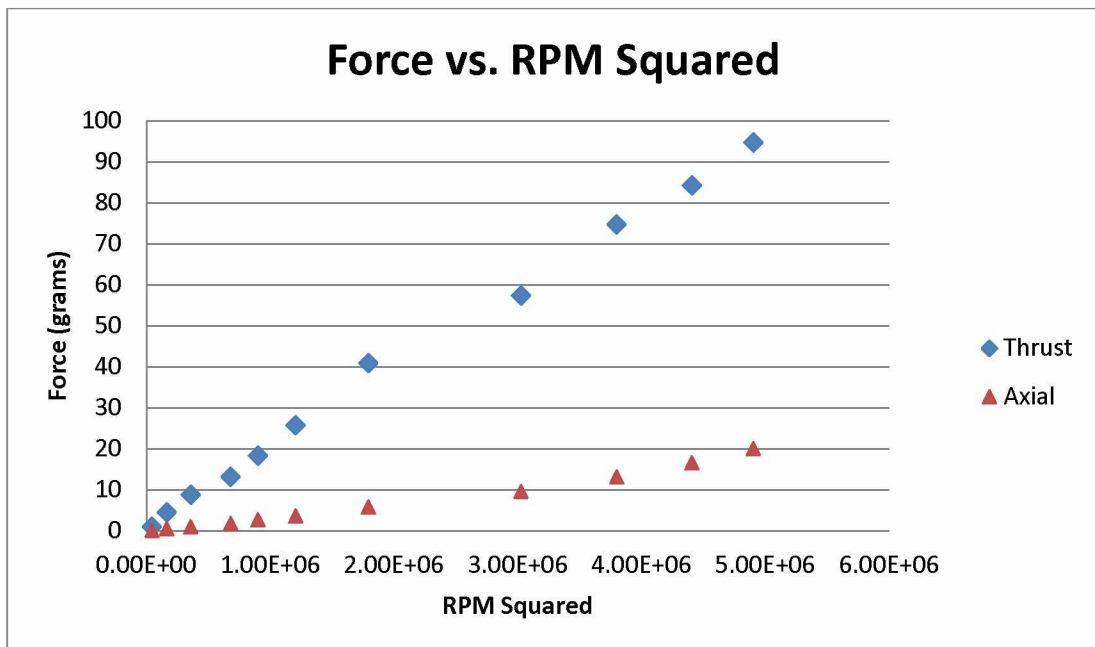


Figure 37: Plot of the two perpendicular forces, thrust (R^2 correlation of 0.9967) and axial force (R^2 correlation of 0.9857) on the rotor as a function of the RPM squared.

Figure 36 shows the forces on the rotor plotted against the RPM of the rotor. The two forces are considered to be independent and orthogonal from one another. At low RPM, the rotor experienced a small force. However, as the speed of the rotor increased the forces on the rotor are proportional to the square of the RPM.

Figure 37 shows the relationship of the two forces to the square of the RPM, and the relationship is quite linear. This is because the forces have a intercept of zero and when the rotor is not moving no force is being generated.

7.2 Cycloidal Rotor Comparison

Table 1, shows the performance of previous cycloidal rotor designs with given dimensions, maximum RPM, and relative flow regime (i.e. Reynolds number). Two recent rotors were developed and tested by the University of Maryland. The second of the two developed recently in 2011 is referred to as the twincyclo and is one of the only flying cycloidal rotors. At 2100 RPM one of the twincyclo's rotors was able to produce 90 grams of thrust which is 7% more thrust at this RPM than the tensile rotor. As the power at this RPM and axial force are unspecified, no other quantitative comparison can be made between them.

Table 1: Showing the performance and geometry of some previous cycloidal rotor designs. Table adapted from the University of Maryland, Department of Aerospace (Chopra, 2011).

	Date	Diameter (cm)	Span (cm)	Number of Airfoils	Maximum RPM	Reynolds Number
Wheatley	1935	243.8	243.8	4	700	5.30E+05
Bosh	1998	121.9	121.9	6	550	6.70E+05
Labiche	2003	60.96	60.96	3	825	1.70E+05
SNU	2004	140.2	100.6	4	500	5.60E+05
SNU	2006	170.7	100.6	4	450	3.40E+05
SNU	2006	39.6	33.53	4	1500	9.50E+04
Tecnion	2003	10.97	10.97	2,4,6	5000	4.00E+04
UMD	2008	15.24	15.24	3,6	2000	1.50E+04
UMD	2011	12.7	12.7	4	2400	2.68E+05
UAF	2012	13.34	13.34	4	2200	2.82E+05

Benedict had also conducted analyses on varying the pitch angle and using a flat plate for airfoils in 2011. This conventional cycloidal rotor cyclically pitched the airfoils on only the free end, and found that there was torsion in the airfoils. The

torsion produced a skewed airflow resulting in an axial air flow and force with relative magnitude of the thrust. The rotor is slightly larger and produces more thrust at a comparable RPM than the tensile rotor. A ratio will be introduced for comparison. The ratio will be a thrust-to-axial-force ratio, where the RPM will be the same for both rotors. The rotor produced 137 grams of thrust and 70 grams of axial force at 2000 RPM with an offset four bar linkage pitching the airfoils using 10% power for mechanical purposes. The tensile cycloidal rotor produced 77.83 grams of thrust and 14.21 grams of axial force with 13% power going towards mechanical purposes using two pitching mechanisms. This gave a force ratio of 1.96 compared to 5.48 in favor of the tensile rotor producing 2.8 times more thrust to axial force.

At lower RPM the conventional rotor is much more efficient due to the increase in power used in the tensile rotor. The conventional rotor produced 9 grams/w where the tensile rotor only produced 2 grams/w at 1200 RPM. Benedict et al. rotor at 2000RPM had a thrust-to-power ratio of 5.3 grams/Watt, where the tensile rotor increased to 3.05 grams/w. The straight airfoil cycloidal rotor ratio of thrust-to-power decreased as the RPM increased. This is characteristic of rotorcraft because the power is proportional to the cube of the RPM where the thrust is only proportional to the square of RPM. To increase the RPM the power increases an order of magnitude greater than the force, causing rotorcraft to be less efficient at higher speeds.

The performance of the tensile rotor did not display this ideal behavior, becoming more efficient as the operating speed of 2200RPM was reached. The lack of performance suggests that there are significant mechanical power requirements to overcome. If the friction could be reduced, the rotor would increase the thrust-to-power ratio and become more efficient at lower RPM. This also leaves improvement for the rotor at all speeds. However, the losses in power are believed to be due to the power required to torque the airfoils as the angle of attack changes. The flat plate airfoils are not able to have a constant pitch along the span, therefore losing power due to the cylindrical geometry.

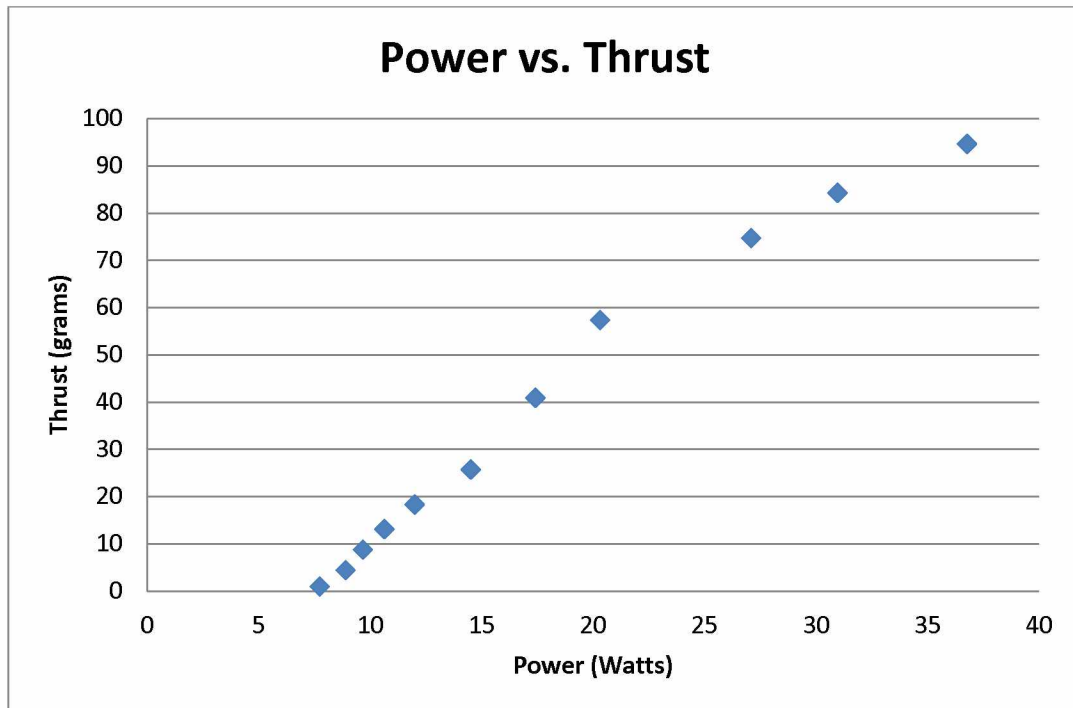


Figure 38: Relationship for total power and thrust as RPM varies.

Figure 38 shows a nonlinearity of decreasing thrust at high power in the power versus thrust of the tensile cycloidal rotor. Each data point is the thrust-to-power relationship at a different RPM. Ideally, zero thrust should be generated for no power input to the rotor. However, 8w was required to produce any thrust from the rotor. This is nearly 20% of the maximum power of the motor at peak efficiency. This additional power draw is believed to decrease because the thrust to power ratio increased as the rotor approached operating speeds.

7.3 Conclusions

Pitching the airfoils on both sides of the rotor caused a decrease in thrust when compared to a conventional cycloidal rotor of similar geometry operating at maximum RPM. The axial force was reduced considerably in comparison to the thrust that was generated of a similar rotor. This reduction in thrust is thought to be due to torsion on both sides of the center of the airfoils.

As both sides of the airfoil are trying to pitch simultaneously the middle of the airfoil does not pitch all the way and instead caused torsion on both sides of the airfoil. Because of the geometry of the airfoils a change in pitch would be needed to change the area of the airfoil. For example, if a positive pitch were to be achieved uniformly, the flat plate airfoil would be required to compress from the quarter chord to the leading edge. Rotating around the quarter chord, the remaining three quarters of the flat plate would need to fan out to achieve a uniform angle of attack. This would require a material that expands and contracts.

The low-thrust-to power ratio at low RPM suggests that there are mechanical power requirements due to friction. This caused a large percentage of the total power to be lost because it was not used for aerodynamic purposes. To increase the thrust the friction would have to be greatly reduced. The power losses are thought to be due to the power required to torque the airfoils as the angle of attack changes. The flat plate airfoils are not able to have a constant pitch along the span resulting in power loss due to the cylindrical geometry.

The low weight of the rotor was compromised because the pitching mechanisms were cast in bronze instead of machined of a much lighter material. This caused the pitching mechanisms alone to weigh 30 grams. The spider supports and airfoils collectively weighed only 8 grams, and could possibly be reduced further. If ceramic bearings and lighter hardware were utilized the overall weight of the rotor may be less than 20 grams. This would allow the rotor to have a better thrust-to-weight output. The thrust that was achieved is greater than the weight of the rotor, and likely sufficient to also accommodate additional structure, and electronics that would be required for flight.

7.4 Further Consideration

A cam cyclic pitching mechanism can be implemented on a conventional cycloidal rotor at the micro-air vehicle scale. Two mechanisms would allow pitching on both sides of the airfoils. This may reduce overall power consumption by 7% when compared to a cycloidal rotor with two four bar pitching mechanisms using 20% of the overall power. This would allow for an increase in efficiency at all operating speeds and potentially allow for a light weight flat plate in place of airfoils. Machining for this type of pitching mechanism would be simple in two dimensions rather than the five as would be required for this tensile rotor.

8 References

- Benedict et al. (2011, January 25-27). Experimental Investigation of the Effect of Rotor Geometry on the Performance of MAV-Scale Cycloidal Rotor. *Proceeding of the International Specialists' Meeting on Unmanned Rotorcraft*. Tempe, AZ.
- Benedict, M., Chopra, I., Ramasamy, M., & Leishman, J. G. (2008). Experimental Examination of the Cycloidal-Rotor Concept for a Hovering Micro Air Vehicle.
- Chopra, B. A. (2011). *Design, Development and Flight Testing of a Twin-Rotor Cyclocopter Micro Air Vehicle*. Department of Aerospace Engineering University of Maryland.
- Clark, R. (2008). Design and Initial Performance of a 500-kW Vertical Axis Wind Turbine.
- Clark, R. (2006). *SBIR A02.07: VTOL to Transonic Aircraft*. Acuity Technologies Proprietary.
- Hein, B. A. (2005, January). Hover Performance of Micro Air Vehicles: Rotors at Low Re. *American Helicopter Society International Specialists' Meeting on Unmanned Rotorcraft*. Arizona.
- Iosilevskii, L. (2003). Aerodynamics of the Cyclogiro. *33rd AIAA Fluid Dynamics Conference and Exhibit*. Orlando: Technion-Israel Institute of Technology.
- Kim, H. A. (2008). *Aerodynamic Performance Enhancement of Cycloidal Rotor According to Blade Pivot Point Movement and Preset Angle Adjustment*. Seoul: School of Mechanical and Aerospace Engineering.
- Kirsten, F. (n.d.). Cycloidal Propulsion Applied to Aircraft Transaction of the AMSE. *AER-50-12*, 25-48.
- McMichael, J. A. (1997, August). *Micro Air Vehicles - Toward a New Dimension*. Retrieved from <http://www.darpa.mil/tto/MAV/mavauvsi.html>
- Parsons. (2005). *Investigation and Characterization of a Cycloidal Rotor for Application to a Micro-Air Vehicle*. Department of Aerospace Engineering.
- Sachse, H. (1926). *Kirsten-Boeing Propeller*. NACA Technical Memorandum.
- Wheatley, J. B. (1933). *Simplified Aerodynamic Analysis of the Cyclogiro Rotating-Wing System*. Washington: Langley Memorial Aeronautical Laboratory.

Appendix A

%
O00592

(FIXTURE Spider Support MAV)
(WRITTEN BY KELSEY ELFERING)
(1-23-12)
(PROGRAM TO CUT SPIDER)
(T8 - 3/8 END MILL)

(G54 XY LEFT EDGE ENTRY POSITION)
(G54 Z 0 TOP OF FIXTURE)

G00 G90 G49 G20

T8 M06 (1/4 CARBIDE MILL)
S6120 M03
G00 G54 X-1. Y3.4237
G43 H8 Z-0.002

(SHORT ROUGH)
G01 X0.9385 Y3.4237
G02 X1.0611 Y3.3861 R0.3538
G03 X1.4483 Y3.2675 R0.5562
G01 X2.1863 Y3.2675
G03 X2.7425 Y3.8236 R0.5562
G01 X2.7425 Y4.5616
G03 X2.6238 Y4.9489 R0.5562
G02 X3.2561 Y4.9489 R-0.3538
G03 X3.1375 Y4.5616 R0.5562
G01 X3.1375 Y3.8236
G03 X3.6936 Y3.2675 R0.5562
G01 X4.4316 Y3.2675
G03 X4.8189 Y3.3861 R0.5562
G02 X4.8189 Y2.7538 R-0.3538
G03 X4.4316 Y2.8725 R0.5562
G01 X3.6936 Y2.8725
G03 X3.1375 Y2.3163 R0.5562
G01 X3.1375 Y1.5783
G03 X3.2561 Y1.1911 R0.5562
G02 X2.6238 Y1.1911 R-0.3538
G03 X2.7425 Y1.5783 R0.5562
G01 X2.7425 Y2.3163
G03 X2.1863 Y2.8725 R0.5562
G01 X1.4483 Y2.8725
G03 X1.0611 Y2.7538 R0.5562
G02 X0.9385 Y3.4237 R-0.3538

(SHORT FINISH)

G01 X0.9385 Y3.4137 F30
G02 X1.0611 Y3.3761 R0.3438
G03 X1.4483 Y3.2575 R0.5662
G01 X2.1863 Y3.2575
G03 X2.7525 Y3.8236 R0.5662
G01 X2.7525 Y4.5616
G03 X2.6338 Y4.9489 R0.5662
G02 X3.2461 Y4.9489 R-0.3438
G03 X3.1275 Y4.5616 R0.5662
G01 X3.1275 Y3.8236
G03 X3.6936 Y3.2575 R0.5662
G01 X4.4316 Y3.2575
G03 X4.8189 Y3.3761 R0.5662
G02 X4.8189 Y2.7638 R-0.3438
G03 X4.4316 Y2.8825 R0.5662
G01 X3.6936 Y2.8825
G03 X3.1275 Y2.3163 R0.5662
G01 X3.1275 Y1.5783
G03 X3.2461 Y1.1911 R0.5662
G02 X2.6338 Y1.1911 R-0.3438
G03 X2.7525 Y1.5783 R0.5662
G01 X2.7525 Y2.3163
G03 X2.1863 Y2.8825 R0.5662
G01 X1.4483 Y2.8825
G03 X1.0611 Y2.7638 R0.5662
G02 X0.9385 Y3.4137 R-0.3438

G43 H8 Z2.0

(NEW ENTRY POSITION RIGHT EDGE)

G00 X12.8 Y2.7162

G43 H8 Z-.002

(LONG ROUGH)

G01 X11.1364 Y2.7162
G02 X11.0139 Y2.7538 R0.3538
G03 X10.6266 Y2.8725 R0.5562
G01 X9.7756 Y2.8725
G03 X9.2195 Y2.3163 R0.5562
G01 X9.2195 Y1.4653
G03 X9.3381 Y1.0781 R0.5562
G02 X8.7058 Y1.0781 R-0.3538
G03 X8.8245 Y1.4653 R0.5562
G01 X8.8245 Y2.3163
G03 X8.2683 Y2.8725 R0.5562
G01 X7.4173 Y2.8725
G03 X7.0301 Y2.7538 R0.5562
G02 X7.0301 Y3.3861 R-0.3538

G03 X7.4173 Y3.2675 R0.5562
G01 X8.2683 Y3.2675
G03 X8.8245 Y3.8236 R0.5562
G01 X8.8245 Y4.6746
G03 X8.7058 Y5.0619 R0.5562
G02 X9.3381 Y5.0619 R-0.3538
G03 X9.2195 Y4.6746 R0.5562
G01 X9.2195 Y3.8236
G03 X9.7756 Y3.2675 R0.5562
G01 X10.6266 Y3.2675
G03 X11.0139 Y3.3861 R0.5562
G02 X11.1364 Y2.7162 R-0.3538

(LONG FINISH)

G01 X11.1364 Y2.7262 F30
G02 X11.0139 Y3.3861 R0.3438
G03 X10.6266 Y3.2675 R0.5662
G01 X9.7756 Y3.2675
G03 X9.2095 Y2.3163 R0.5662
G01 X9.2095 Y1.4653
G03 X9.3281 Y1.0781 R0.5662
G02 X8.7158 Y1.0781 R-0.3438
G03 X8.8345 Y1.4653 R0.5662
G01 X8.8345 Y2.3163
G03 X8.2683 Y3.2675 R0.5662
G01 X7.4173 Y3.2675
G03 X7.0301 Y3.3861 R0.5662
G02 X7.0301 Y2.7538 R-0.3438
G03 X7.4173 Y2.8725 R0.5662
G01 X8.2683 Y2.8725
G03 X8.8345 Y3.8236 R0.5662
G01 X8.8345 Y4.6746
G03 X8.7158 Y5.0619 R0.5662
G02 X9.3281 Y5.0619 R-0.3438
G03 X9.2095 Y4.6746 R0.5662
G01 X9.2095 Y3.8236
G03 X9.7756 Y2.8725 R0.5662
G01 X10.6266 Y2.8725
G03 X11.0139 Y2.7538 R0.5662
G02 X11.1364 Y2.7262 R-0.3438
G91 G28 Z0
G28 Y0
G90
M30
%

Appendix B Electronic Specifications

Controller:

Features:

2.4ghz FHSS Technology

Dual Rate

Fail Safe

HKR3000 3ch RX (Included)

Detailed User manual

Required: 8 x AA Batteries



ESC/BEC:

Built with imported N-Channel mosFETs and an ultra fast Atmel MCU & heartbeat make this a high performance ESC with excellent sync capabilities. This ESC has a 4A SBEC for solid reliable servo power.

Programmable via an R/C controller. It allows you to program all functions to fit your specific needs, which makes it efficient and user friendly.

Features:

Extremely low internal resistance

Super smooth and accurate throttle linearity

Over heat and over-load protection

Auto shut down when signal is lost or radio interference becomes severe for more than 2 seconds

Supports high RPM motors

Power arming protection (prevents the motor from accidentally running when switched ON)

New Advanced programming software

Soft Acceleration Start Up: Medium

Governor mode : OFF

Frequency : 8kHz

Low voltage cutoff type: Reduce power

Cont. Current: 40A

Burst Current: 60A

Battery: 2-6 Cell Lipo / 5-18 Cell Ni-XX

SBEC: 5.5V/ 4A Output

Size: 52*23*7mm

Weight: 30g

Battery:

Pack Dimensions: 24x34x62mm
 Pack Weight : 115grams (20C)
 Capacity : 1300mAh+ (usually underrated by 100mAh)
 Cycle Life : 250~300 Cycles

Receiver:

HK-3000 3ch 2.4GHz FHSS RX
 Weight: 9g
 Dimensions: 40mm x 27mm x 13mm
 Antenna Length: 180mm

**Motor:**

Dimension: 17.8mm x 24mm
 Weight: 7.9g /0.28oz (not including mount)
 Diameter of shaft: 2.0mm
 Length of front shaft: 6mm
 KV: 2900
 Unload current: 11.1v 0.5A
 Max Load: 5.1A

